

Perceiving, Predicting, and Planning: Robotic Expeditionary Science in Spatiotemporal Fields

by

Victoria Lynn Preston

B.S., Olin College of Engineering (2016)

S.M., Massachusetts Institute of Technology (2019)

Submitted to the Department of Aeronautics and Astronautics
and the Joint Program in Applied Ocean Science and Engineering
in partial fulfillment of the requirements for the degree of

Doctor of Philosophy

at the

MASSACHUSETTS INSTITUTE OF TECHNOLOGY

and

WOODS HOLE OCEANOGRAPHIC INSTITUTION

February 2023

© 2023 Victoria Lynn Preston. All rights reserved.

The author hereby grants to MIT permission to reproduce and to distribute publicly paper
and electronic copies of this thesis document in whole or in part in any medium now
known or hereafter created.

Author
Department of Aeronautics and Astronautics, MIT

Applied Ocean Science and Engineering, WHOI

December 15, 2022

Certified by
Nicholas Roy

Bisplinghoff Professor of Aeronautics and Astronautics, MIT
Thesis Supervisor

Certified by
Anna Michel

Associate Scientist with Tenure, Applied Ocean Physics and Engineering, WHOI
Thesis Supervisor

Accepted by
Jonathan P. How

R. C. Maclaurin Professor of Aeronautics and Astronautics, MIT
Chair, Graduate Program Committee

Accepted by
David Ralston

Associate Scientist with Tenure, Applied Ocean Physics and Engineering, WHOI
Chair, Joint Committee on Applied Ocean Science and Engineering

Perceiving, Predicting, and Planning: Robotic Expeditionary Science in Spatiotemporal Fields

by

Victoria Lynn Preston

Submitted to the Department of Aeronautics and Astronautics and the Joint Program in Applied Ocean Science and Engineering on December 15, 2022, in partial fulfillment of the requirements for the degree of Doctor of Philosophy.

Abstract

Context:

Importance:

How:

Challenge:

Intuition/Thesis Statement:

How Intuition was Applied:

Results:

Impact:

Making measurements of the natural world and building accurate models is crucial to understanding our environment and the spatiotemporal processes that drive our climate. Autonomous robots are especially well-suited to gathering those measurements efficiently. However, to collect useful observations of unknown, partially-observed spatiotemporal distributions for scientific inquiry requires accurately perceiving a phenomenon of interest, predicting how it will evolve in time, and planning effective sampling trajectories, potentially under severe operational constraints.

This talk will present the problem of deep-sea hydrothermal plume charting with an autonomous underwater vehicle (AUV) as part of an oceanographic research expedition. In this setting, the AUV, by matter of policy and ability, is operationally restricted to executing pre-set, fixed trajectory patterns (i.e., the robot's behavior cannot respond to observations). Yet, the AUV is tasked with densely surveying the spatiotemporal structure of an a priori unknown moving geochemical field, the state of which is only partially-observable and subject to unseen forces (e.g., advective current, diffusive mixing). To enable this capability for an AUV, I will describe a deployment-by-deployment iterative learning and trajectory optimization process, PHORTEX: Physically-informed Operational Robotic Trajectories for Expeditions. In this process we learn to predict the state of the spatiotemporal plume from a history of partial scientific measurements by embedding idealized scientific priors (e.g., analytical models of plume rise) in a Bayesian inference framework. I will present results from 2021 field experiments at a deep sea (2000 m) hydrothermal vent field in the Gulf of California using AUV Sentry.

Thesis Supervisor: Nicholas Roy
Title: Bisplinghoff Professor of Aeronautics and Astronautics, MIT

Thesis Supervisor: Anna Michel
Title: Associate Scientist with Tenure, Applied Ocean Physics and Engineering, WHOI

Acknowledgments

Thank you, everyone.

Contents

1	Introduction	17
2	Problem Setting	19
2.1	Science Background	21
2.2	Robotics Background	21
3	Perceiving Spatiotemporal Phenomena	23
3.1	Discovering Hydrothermalism from Afar	23
3.2	Materials and Methods	26
3.2.1	Site Description	26
3.2.2	Sampling Platforms and Instruments	28
3.2.3	Analytical Procedure	32
3.2.4	Transect Design and Execution	32
3.3	Results	34
3.3.1	Methane Observations from Spectroscopic Instruments	34
3.3.2	Methane and Ammonium Observations with the Rosette	34
3.3.3	Turbidity	35
3.3.4	Oxidation Reduction Potential	37
3.3.5	Temperature, Salinity, and Oxygen	38
3.4	Discussion	40
3.4.1	Sensor Cross-Correlations	40
3.4.2	Hydrothermalism Detection via Time-Series Regimes	43
3.4.3	Methane in Deep Sea Exploration	45

3.4.4	Enabling Better Decision-Making for Hydrothermalism Discovery	47
3.5	Interpreting Point Observations of Hydrothermal Fluids	48
3.6	Leveraging Sensors of Opportunity	49
3.7	Summary	49
4	Predicting: Representing Belief and Simulating Uncertain Dynamics	51
4.1	General Models: GPs	51
4.2	Embedded Physical Models: PHUMES	51
4.3	Physically-Informed Learned Models: PIKL	51
4.4	Performance in Hydrothermal Domains	51
4.5	Summary	51
5	Planning: Adaptive Sampling in Spatiotemporal Fields	53
5.1	Underway Autonomy: PLUMES	53
5.2	Deployment-by-Deployment Autonomy: PHORTEX	53
5.3	Field Results in GB	53
5.4	Summary	53
6	Discussion	55
6.1	Generalizing to Other Domains	55
6.2	Open Challenges	55
6.3	Embedding Autonomy Engineers into Science Teams	55
6.4	Robotics in Expeditionary Science	55
7	Looking Forward	57
A	Perceiving: Supplemental Information	59
A.1	Method for Methane Measurement from Niskin Bottles	59
A.2	Leg 2 Niskin Bottle Sample Schedule and Measurements	61
A.3	Normalized Pythia Calibration	62
A.4	Depth-Correction	63

A.5 Description of Plume Model for Transect Design	64
--	----

List of Figures

3-3	The SAGE and Pythia instruments mounted on the rosette and AUV <i>Sentry</i> , respectively.	30
3-4	Normalized methane values observed with both SAGE (rosette) and Pythia (<i>Sentry</i>) over reference distance from (27.407489 N, 111.389893 W). The transect begins at the left of the plot and proceeds to the right. Strong methane anomalies, defined as points above a conservative threshold of 0.5 normalized values, are present starting 3 km from the reference source as observed by Pythia, and 1.5 km as observed by SAGE (open green circles).	35
3-5	Normalized methane measurements by SAGE plotted with methane measurements taken from Niskin bottle samples (as measured by DGEU/GGA equipment) and ammonium measurements. Bottle methane measurements are reported as a range to reflect sensitivity of the measurement procedure to a calibrated extraction efficiency. All measurements trend towards a peak observation of methane and ammonium 0.75 km from the reference source. SAGE additionally observes a secondary peak approximately 2 km from the source, which is essentially missed by the bottle sample schedule.	36
3-6	Turbidity observed as beam attenuation on the rosette transmissometer and optical backscatter on AUV <i>Sentry</i> instruments. <i>Sentry</i> encountered a sensor error until approximately 4.5 km from the ridge reference point. After this point, elevated turbidity is detectable throughout the dive, with significant elevations within 3.3 km east of the ridge reference point, dissipating within tens of meters to the west. Elevated turbidity is observed by the rosette 2.2 km from the ridge reference point to the east.	37
3-7	The derivative of ORP observed by data collected on AUV <i>Sentry</i> . Negative slopes are indicative of entering hydrothermal fluids. Only one region of the transect demonstrated a significant reaction to ORP, within 200 m of the reference point.	38

A-1 Fitted calibration curve for measurements of methane observed by Pythia.	63
A-2 Calibration curve, smoothing, and time correction applied to Pythia observations during the transect, before reported normalization in the manuscript.	64
A-3 Linear functions are fit to data collected for oxygen, temperature, and salinity instruments on each platform separately. A residual value is then computed for each observation.	64
A-4 A prototypical plume estimate according to the modified buoyant plume model in crossflow. The same envelope is plotted with respect to absolute depth (with a source located at 1850 m) on the left, and illustratively in the context of the hydrothermal ridge on the right.	67

List of Tables

A.1	Results of DGEU extraction efficiency calibration experiments.	61
A.2	Schedule of bottle samples during Leg 2 of rosette trajectory.	62
A.3	Geochemical measurements associated with the schedule of bottle samples during Leg 2 of rosette trajectory. Note that methane expressed in nM is computed using coincident temperature and salinity measurements during the transect as measured by rosette CTD, and extraction inefficiency of the DGEU is compensated for as described in Sec. A.1.	62
A.4	Parameter, vent characteristics, and ambient crossflow setting used for transect design.	67

Chapter 1

Introduction

The environmental sciences are a multidisciplinary endeavor to understand the Earth, its ecosystems, and its processes, for which *in situ* observational studies or *expeditions* serve as the foundation on which scientific discovery and model development is predicated. Robots are uniquely well-positioned to advance long-term monitoring of and exploration in meso-scale planetary environments through autonomous expeditions. By virtue of their form, robots can be used in extreme places (e.g., deep sea), dangerous scenarios (e.g., edge of calving ice sheets), or long-term missions (e.g., Mars exploration). Increasingly, robotic platforms are being developed for scientific expeditions, but their autonomous capabilities are typically limited to predetermined hand-designed trajectories (e.g., uniform coverage lawnmowers [Camilli et al., 2010]). This significantly restricts the class of phenomena that can be effectively studied by expeditionary scientific robots. For instance, spatiotemporal distributions—deep sea hydrothermal plumes, algal blooms, weather cells—can be severely under-sampled or missed using these strategies [Flaspoehler et al., 2019]. Given the ubiquity of these spatiotemporal phenomena and the cost of scientific field operations, it is critical to improve the efficacy of robots as autonomous scientific tools.

This thesis represents...

Chapter 2

Problem Setting

To collect useful samples of a spatiotemporal field using a robotic platform is to pose a *sequential decision-making* problem. In this setting, we assume that the measurements that can be collected are partial observations of the unknown spatiotemporal environment, and the actions the robot can take in sequence are operationally constrained. We can formally state this problem as a partially observable Markov decision process (POMDP). Let $\Pi(\cdot)$ denote the space of probability distributions over the argument. A finite horizon POMDP can be represented as tuple: $(\mathcal{S}, \mathcal{A}, T, R, \mathcal{Z}, O, b_0, H, \gamma)$, where \mathcal{S} are the states, \mathcal{A} are the actions, and \mathcal{Z} are the observations. At planning iteration t , the agent selects an action $a \in \mathcal{A}$ and the transition function $T : \mathcal{S} \times \mathcal{A} \rightarrow \Pi(\mathcal{S})$ defines the probability of transitioning between states in the world, given the current state s and control action a . The transition function governs both how the state of the robot will evolve, given a chosen action, and the potentially stochastic evolution of the underlying spatiotemporal environment. After the state transition, the agent receives an observation according to the observation function $O : \mathcal{S} \times \mathcal{A} \rightarrow \Pi(\mathcal{Z})$, which defines the probability of receiving an observation, given the current state s and previous control action a . The reward function $R : \mathcal{S} \times \mathcal{A} \rightarrow \mathbb{R}$ serves as a specification of the task, assigning the states of the world that are useful for a given scientific objective high reward and others low reward. A POMDP is initialized with belief $b_0 \in \Pi(\mathcal{S})$ — an initial probability distribution over state — and plans over horizon $H \in \mathbb{Z}^+$ with discount factor

$$\gamma \in [0, 1].$$

As the robot moves through the world, it selects actions and receives observations. Since the state of the world is not directly observable in a POMDP, the robot maintains a probability distribution over possible states (i.e., belief) and must update this distribution each time it takes an action and receives an observation. Given the transition and observation models, the belief can be updated directly using Bayes rule using a Bayes filter [Särkkä, 2013]:

$$\tau(b_{t-1}, a_{t-1}, z_t) = b_t \triangleq \Pi(S_t | a_0, z_0, \dots, a_{t-1}, z_{t-1}, z_t) \quad (2.1)$$

$$= \Pi(S_t | b_{t-1}, a_{t-1}, z_t) \quad (2.2)$$

$$= \frac{\int_{s \in \mathcal{S}} O(s, a_{t-1}, z_t) T(s, a_{t-1}, s') b_{t-1}(s')}{\Pi(z_t | b_{t-1}, a_{t-1})} \quad (2.3)$$

where $\tau(b, a, z)$ is the updated belief after taking control action a and receiving observation z (Eq. (2.3)). Unfortunately, Eq. (2.3) is intractable to compute directly and an approximate Bayesian inference procedure is required to represent the belief (e.g., Kalman filter [Welch et al., 1995], particle filter [Silver and Veness, 2010], or variational methods).

Due to the stochastic, partially observable nature of current and future states, the realized reward in a POMDP is a random variable. Optimal planning is defined as finding a horizon-dependent policy $\{\pi_t^* : \Pi(\mathcal{S}) \rightarrow \mathcal{A}\}_{t=0}^{H-1}$ that maximizes expected reward: $\mathbb{E}\left[\sum_{t=0}^{H-1} \gamma^t R(S_t, \pi_t(b_t)) | b_0\right]$, where b_t is the updated belief at time t , conditioned on the history of actions and observations. The recursively defined horizon- h optimal value function V_h^* quantifies, for any belief b , the expected cumulative reward of following an optimal policy over the remaining planning iterations:

$$V_0^*(b) = \max_{a \in \mathcal{A}} \mathbb{E}_{s \sim b}[R(s, a)] \text{ and}$$

$$V_h^*(b) = \max_{a \in \mathcal{A}} \mathbb{E}_{s \sim b}[R(s, a)] + \gamma \int_{z \in \mathcal{Z}} \Pi(z | b, a) V_{h-1}^*(\tau(b, a, z)) dz \quad h \in [1, H-1], \quad (2.4)$$

The optimal policy at horizon h is to act greedily according to a one-step look ahead of

the horizon- h value function. However, Eq. (2.4) is intractable for large or continuous state, action, or observation spaces and thus the optimal policy must be approximated. Much of the art of practical decision-making uncertainty is making well-designed algorithmic and heuristic choices that enable efficient and robust planning algorithms.

2.1 Science Background

2.2 Robotics Background

Chapter 3

Perceiving Spatiotemporal Phenomena

To track a spatiotemporal phenomenon first requires sensing it. Expeditionary robots, in addition *ex situ* analysis containers for species collection, are typically equipped with a suite of heterogeneous *in situ* sensors with varying field of views, accuracies, and noise models. In geochemical contexts in marine environments, these *in situ* sensors tend to yield continuous point observations for a proxy field (e.g., temperature, pressure, oxygen concentration), rather than precise measurements of an aggregate phenomenon (e.g., the presence of plume).

3.1 Discovering Hydrothermalism from Afar

Detecting and characterizing seafloor hydrothermal vents is critical in understanding the fundamental interactions among the geochemical and biological processes on the seafloor, and the fluxes that these processes cause to and from the deep ocean. Since the first discovery of deep sea hydrothermalism in 1977 ([Corliss et al., 1979]), hundreds of hydrothermal venting sites have been discovered and analyzed ([Beaulieu et al., 2015]). These studies reveal that hydrothermal vents play a major role in ocean-scale elemental and micronutrient budgets (e.g., ([Le Bris et al., 2019, Resing et al., 2015])), serve as nutrient pumps to the deep ocean (e.g., [Dick et al., 2013, Vic

et al., 2018, Scholz et al., 2019, Bell et al., 2017]), and sustain abundant and unique (e.g., chemosynthetic) forms of complex life ([Grassle, 1987, Georgieva et al., 2021]). Hundreds of vent sites are hypothesized to exist and yet remain undiscovered in the deep ocean ([Beaulieu et al., 2015]), limiting efforts to constrain nutrient and energy budgets of the deep ocean, to assess the magmatic budget hypothesis which estimates the global stock of hydrothermal activity, and to understand these novel ecosystems.

Exhaustive search of the seafloor is an impractical method for discovering new vents due to the scale of the ocean environment. Instead, adaptive surveying strategies and novel sensing technologies can be combined to detect hydrothermalism far (over 1 km laterally) from the plume source using water column observations. Hydrothermal plumes form due to a density difference between background seawater and (often significantly) heated vent fluids. The resulting buoyant force creates a coherent rising stem from the vent (the buoyant stem) and a spreading cloud (the neutrally-buoyant layer) at an isopycnal, when the cooling, mixing, hydrothermally-derived fluids reach equivalent density to the ambient background ([Morton et al., 1956, Speer and Rona, 1989]). The chemical composition of hydrothermal fluids differs greatly from that of background seawater and the plume-derived fluids near an active vent can be detected using most standard properties (i.e., temperature, salinity, chemical composition, turbidity). However, the spatial expression of the buoyant plume stem is typically no more than a few tens of square meters, making the buoyant stem difficult to localize on a survey. As emitted fluids travel further within the plume, the physically and chemically distinctive nature of the hydrothermal water mass is rapidly diluted as the plume entrains background seawater. Throughout this advective evolution of the plume, reactive (non-conservative) tracers can be consumed or transformed. Thus, despite the neutrally buoyant layer having a spatial scale extending for several square kilometers, detecting these plume fluids requires innovation in sensing and data analysis.

In this paper, we discuss the potential for water column-based hydrothermal plume discovery using standard sensing equipment (e.g., CTD, optode, transmissometer) in concert with two novel *in situ* methane instruments installed onboard an autonomous

underwater vehicle (AUV) and a towed rosette. We present results from a field deployment at the northern Guaymas Basin in November 2021 and use these results to inform the planning of informative plume transects and the monitoring of real-time instrument responses. Both towed rosettes and AUVs are well-established tools for hydrothermal plume surveys. Rosettes deployed for hydrothermal plume hunting are typically used in either a vertical transect mode, or cast, performed at regularly spaced spatial waypoints along a ship transect, or a “towed” mode, in which the CTD is lowered and pulled through the water by the ship’s motion (e.g., [Chin et al., 1994, Bennett et al., 2013]). AUVs, by virtue of being untethered from the ship, have the ability to finely control location within the water volume, and can typically operate closer to the seafloor than a towed rosette. Standard sensors mounted on either a rosette or AUV can detect different forms of hydrothermalism. High turbidity several hundred meters from the seafloor may be indicative of a neutrally-buoyant plume generated by a black smoker, whereas changes in oxidation-reduction potential and clear waters near the seafloor may be indicative of diffuse flow. Analyzing these sensors individually and in combination can disambiguate these types of hydrothermalism and elucidate plume structure and characteristics of venting sources on the seafloor.

In 2021, our expedition aboard the R/V *Roger Revelle* (RR2107) with AUV *Sentry* and ROV *JASON*, offered a unique opportunity to examine the emission of hydrothermally derived fluids, their buoyant rise, as well as the evolution and fate of the neutrally-buoyant plume in the mid-water. Here, we present the results of a targeted lateral transect using chemical sensors mounted on AUV *Sentry* and a towed rosette, including novel *in situ* methane instruments demonstrated for the first time in the field here. Fig. 3-1 illustrates the overall design of the transect experiment. We show that methane acts as a reliable indicator of hydrothermal activity in the northern Guaymas Basin on a spatial scale of 1.5-3 km at 100-150 m altitude. Methane performed similarly to standard turbidity sensors in this trial (detection 2.2-3.3 km), more sensitively than oxidation reduction potential, and more clearly than temperature, salinity, and oxygen instruments which readily responded to physical mixing in background seawater. We additionally examine the relationships between differ-

ent sensing modalities, and demonstrate how real-time cross correlative or time-series regime identification could be used to assist in survey design for future exploratory missions.

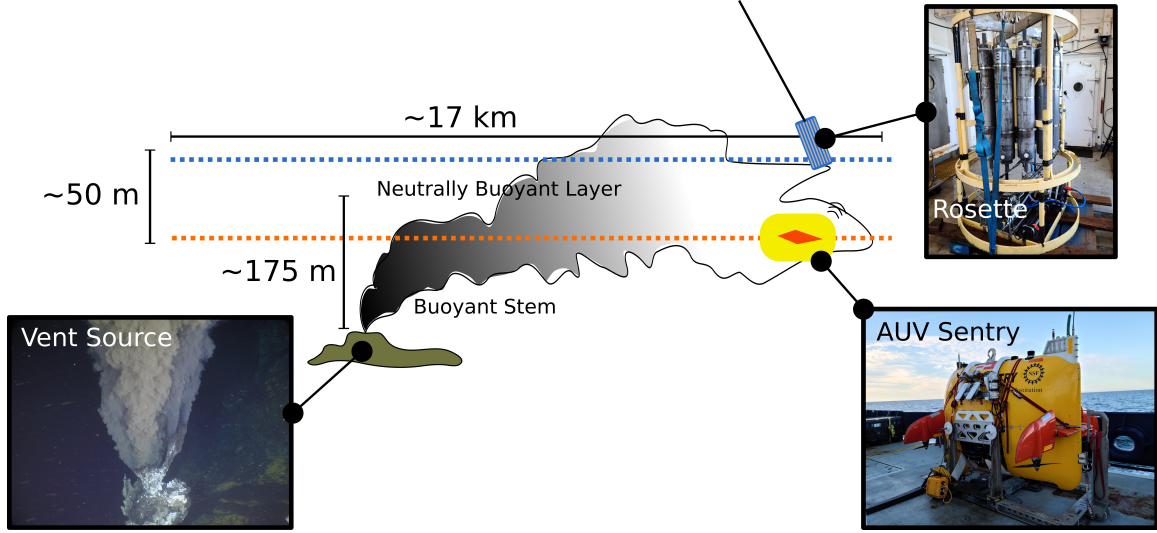


Figure 3-1: Overview of general transect design. Plumes generated by black smoking chimneys at an active hydrothermal ridge in the Northern Guaymas Basin (one example pictured here, taken with an arm mounted MISO camera by ROV *JASON* during RR2107) rise approximately 175 m in the water column and are advected and turbulently mixed with background seawater. AUV *Sentry* and a towed CTD rosette, both equipped with turbidity, oxygen, temperature, salinity, and methane probes, fly trajectories that aim to intersect the lower and upper neutrally buoyant plume layer, respectively. A comparison of the observations collected by both platforms is then used to demonstrate the efficacy of various sensors and algorithmic detection schemes.

3.2 Materials and Methods

3.2.1 Site Description

Located in the central Gulf of California (Mexico), the Guaymas Basin is a mid-ocean ridge extensional spreading center system, with the unique characteristic of being heavily overlain with high amounts of organic-rich sediment. While the primary spreading center axis trends southwest to northeast, the axis of the spreading center in the more well-studied southern end does not extend linearly northeastward, with the northern end of the axis offset to the northwest. The subseafloor eruption

and emplacement of lava into the heavy sediment overburden gives rise to a unique set of hydrothermal characteristics. Among these, the geochemical composition of the emergent fluids and volatiles is highly enriched in dissolved organic compounds, carbon dioxide (CO_2), hydrogen (H_2), ammonium (NH_4^+), and methane (CH_4) ([Seewald et al., 1994, Von Damm et al., 1985]). While the southern end of the basin has been the subject of a long history of geochemical and biological examination (e.g., [Ondréas et al., 2018, Teske et al., 2016, Seewald et al., 1994, Von Damm et al., 1985, Lonsdale and Becker, 1985]), hydrothermal activity was only recently documented along the northern end of the basin at a 600 m long ridge located at a depth of 1850 m ([Soule et al., 2018, Geilert et al., 2018]). Several tall sulfide chimneys 10-25 m in height are located along the ridge, and emit fluids highly-enriched in CO_2 , H_2 , CH_4 among others (Fig. 3-2). The black smoker vents associated with these chimneys consist of clusters of tens of small ($<0.01 \text{ m}^2$) orifices, emitting turbid fluids heated to over 340°C , as observed during RR2107 by ROV *JASON*. In this work, we use the closest identified chimney to the transect trajectories at (27.407489 N, 111.389893 W) as a spatial reference point.

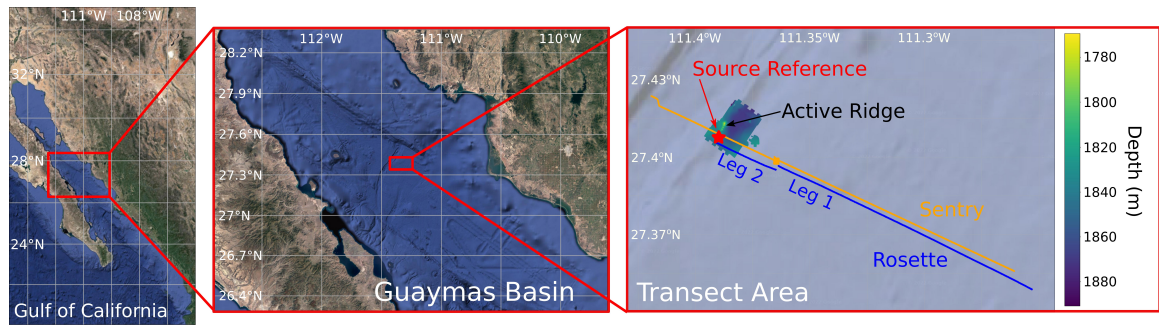


Figure 3-2: AUV *Sentry* and a towed rosette were used to perform coincident several kilometer long trajectories in the Northern Guaymas Basin. The rosette was redeployed mid-trajectory in order to empty the Niskin bottles onboard; this split the rosette trajectory into Leg 1 and Leg 2. The trajectories intersected a region of known hydrothermal activity in the northern basin; a bathymetric relief of this region is overlaid on the far right panel. The red star on the bathymetric relief marks the nearest point of identified hydrothermal activity (black smokers) relative to the trajectories (27.407489 N, 111.389893 W), and is used as a reference point in this work. Imagery is provided by the GoogleTiles API in Cartopy. The bathymetric relief is rendered using data collected by AUV *Sentry* during research cruise RR2107.

3.2.2 Sampling Platforms and Instruments

During expedition RR2107, AUV *Sentry* and a towed rosette were deployed to perform a multi-kilometer transect. Two novel *in situ* methane instruments were deployed during the transect, one on *Sentry*, and the other on the towed rosette. Physical water samples collected by the Niskin bottles on the rosette were processed shipboard to measure both methane and ammonium content. To increase the total number of bottle samples that could be collected over the transect, the towed rosette was deployed and recovered twice; we will refer to the rosette transect before the first recovery as “Leg 1” and after re-deployment as “Leg 2.” AUV *Sentry* was placed in a holding pattern when the rosette was on the ship deck to ensure that spatial measurements between the platforms were temporally comparable.

AUV *Sentry*

AUV *Sentry* executes pre-set trajectories (encoded as a set of waypoints) once underway. During this transect, a starting point at (27.345152 N, 111.253108 W) and ending point at (27.460812 N, 111.527694 W) were given, and a holding pattern was programmed to be executed when the rosette was on the ship deck for sample retrieval after Leg 1. This holding pattern was centered at (27.39592 N, 111.3674 W) and was a lawnmower (back and forth) pattern of approximate dimensions 225 m x 225 m with 15 m resolution. The standard scientific instrumentation deployed on *Sentry* include an oxygen optode (Aanderaa 4330F), an optical backscatter sensor or OBS (Seapoint Turbidity Meter), an oxidation-reduction potential sensor or ORP (NOAA), a CTD (SeaBird SBE49), and 7000 m rated pressure sensor (Paroscientific 8B7000-I). The Pythia instrument (described in Sec. 3.2.2) was additionally installed onto *Sentry* for the transect.

Towed Rosette

During the transect, the rosette was equipped with an ultra-short baseline (USBL) acoustic transceiver to allow the real-time position of the rosette to be tracked with

respect to the ship. Scientific instruments mounted on the rosette included a transmissometer (C-Star), a 6000 m rated CTD (SeaBird SBE 911plus), twelve 10 L Niskin sampling bottles, and an oxygen optode (Aanderaa). The SAGE instrument (described in Sec. 3.2.2) was also fixed to the rosette for the transect. Default instrumentation on the rosette was communicated via the winch cable to the rosette watchstander station in the computer lab onboard the ship. Ship speed was set to $\sim 0.5 \text{ m s}^{-1}$ (~ 1 knot) to assist in controlling rosette depth and winch tension. Niskin bottles were fired according to a schedule that favored more bottles near the ridge. A scheduled stop approximately 3 km from the ridge was used to collect samples from twelve full Niskin bottles and re-deploy the rosette to take an additional twelve bottle samples from the stop to the end of the transect.

Dissolved Methane Analysis with Laser-Based Spectroscopy A Los Gatos Research (LGR) Dissolved Gas Extraction Unit (DGEU) and coupled LGR Greenhouse Gas Analyzer (GGA) were used to measure dissolved methane in seawater collected by Niskin sampling bottles fired during the transect. The DGEU uses a membrane contactor for dissolved gas extraction. Extracted gas is then pumped to the GGA which uses off-axis integrated cavity output spectroscopy for making 1 Hz, precise (<2 parts per billion) measurements of methane in the measurement range of 0-1000 ppm. Extraction of gas is imperfect by the DGEU, and so we apply an extraction efficiency correction of 2.3-3.3% (for calibration details, see Appendix A.1). Methane measurements in ppm are subsequently converted to nanomolar (nM) using coincident salinity and temperature measurements observed by the rosette CTD. Calibration of the GGA was completed using gas standards from Mesa Gas ([Michel et al., 2021]). During the transect, nine of the twelve bottles from Leg 2 were processed using the DGEU and GGA for methane analysis.

Ammonium Measurement Concentrations of ammonium (NH_4^+) were determined onboard within 6 hours of collection from the Niskin bottles following the OPA method ([Holmes et al., 1999]) in a 1 cm cell using an Aquafluor Field Fluorom-

eter (Turner Designs). Standards were prepared using Milli-Q and surface sea water, and then corrected for matrix effects following [Taylor et al., 2007]. Analytical precision was 5 nM, with a detection limit of 1 nM. Ten of the twelve Niskin bottles were processed in this way during Leg 2 of the rosette transect.

Methane Sensors

Two novel sensors for *in situ* methane observation were deployed on the rosette and AUV *Sentry*. The Sensor for Aqueous Gases in the Environment (SAGE) was deployed on the rosette and a real-time cavity ringdown spectrometer called Pythia, was deployed on AUV *Sentry* (Fig. 3-3). Both instruments were in active development during this cruise, and so we report all measurements from these instruments as normalized observations (this can be interpreted as a sensor “saturation” value) in lieu of calibrated concentrations. For the purposes of the analyses herein, there is no loss of generality in the methods proposed to detect hydrothermalism using these normalized values.

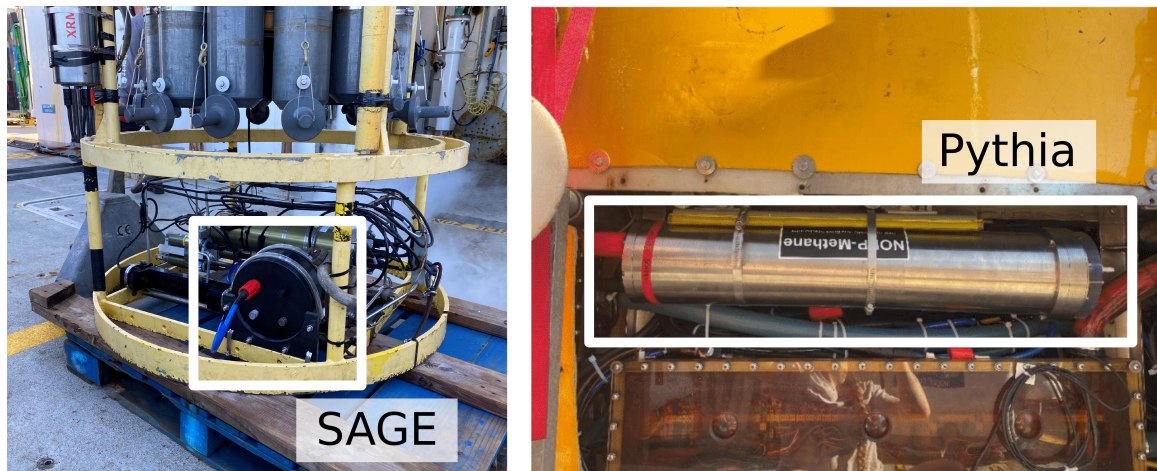


Figure 3-3: The SAGE and Pythia instruments mounted on the rosette and AUV *Sentry*, respectively.

SAGE SAGE is a dissolved gas sensing technology developed at the Woods Hole Oceanographic Institution (WHOI), and this expedition served as the first at-sea validation of the sensor’s operation. SAGE technology has been previously described

in [Kapit and Michel, 2021a, Kapit and Michel, 2021b]. Briefly, SAGE is based on infrared absorption spectroscopy performed on extracted gas from seawater via a gas permeable (and water impermeable) membrane. Once the gas enters the sensor, it fills a hollow-core optical fiber (HCF) which also guides light from a laser source tuned to measure the gas species of interest. The amount of target gas present is determined by measuring the amount of light absorption through the HCF using a photodetector. This prototype version of SAGE was configured to measure methane in the range of 0-10,000 ppm. The resolution of the sensor is <1 ppm. The response time for the deployed configuration was approximately 12 minutes, and the instrument was minimally sensitive to temperature for the scales shown in this paper, (i.e., <2% of the full scale of the observed signal). SAGE is 5.5" long with a 9" outer diameter, and the power requirement was 7 W during this field deployment.

Pythia Pythia is a novel deep-sea methane sensor developed utilizing real-time cavity ringdown spectroscopy (rt-CRDS) developed by WHOI ([Michel et al., 2022]) and Ring-IR Inc. ([Harb et al., 2012]), and capable of operating to 4000 m depths. Pythia extracts dissolved gas from sea water using a large (113 cm^2) surface area membrane. The extracted sample gas enters an optical cell where it is interrogated by a pulsed mid-infrared Quantum cascade laser (QCL). The laser light is absorbed by methane present in the cell, and the concentration of methane is determined by monitoring the pulsed ringdown signal from the cell using a mercury cadmium telluride (MCT) detector. While the response time of the sensor is slow, on the order of 35 minutes, the sensor is responsive to small (<2 ppm) changes in methane; the temperature sensitivity of Pythia has not yet been characterized. Pythia is ideally suited for long dives in environments in which changes to the methane concentration vary over long temporal and spatial scales. Details on the process for normalizing Pythia observations (which are strongly nonlinear and additionally require time correction) are provided in Appendix A.3. Pythia is 24" long with a 4.5" outer diameter, and was operated at a power range between 30-50 W during this field deployment.

3.2.3 Analytical Procedure

Observations collected by sensors deployed on AUV *Sentry*, including Pythia, were merged into a single dataframe using a common 1 Hz time reference; data were linearly interpolated onto this common time reference if they did not share an exact timestamp. With the exception of the derivative of ORP signal, all data for the purposes of visualization is smoothed using a centered rolling average over 5 minute intervals. Additionally, temperature, oxygen, and salinity measurements are normalized with respect to depth (as these quantities are anticipated to be functions of depth in the weakly stratified deep waters). Depth correction is performed by fitting a linear function to the average observation collected in 20 m wide depth-bins, and computing the residuals of all data points with respect to this line (see Appendix A.4 for plots of the linear functions). Rosette data is treated in the same fashion as *Sentry* data. Down-cast and up-casts are removed from both *Sentry* and rosette data streams for all visualizations.

3.2.4 Transect Design and Execution

AUV *Sentry* and the rosette were deployed in the basin approximately 16 km from the northern hydrothermal ridge structure, at (27.348152 N, 111.253108 W) with a course of 295° set to intersect the southern part of the ridge (Fig. 3-2). The *Sentry* trackline was placed approximately 200-300 m north of the rosette to avoid any risk of entanglement. *Sentry* was set in altitude hold mode, targeting 120 m from the bottom (this places *Sentry* at a depth of approximately 1750-1700 m, and at the top of its altitude-hold range). Rosette depth was targeted to be approximately 1650-1600 m, controlled primarily by the speed of the ship and length of the winch cable. These depths were designed based on an estimated model of the neutrally buoyant plume layer, as described in Sec. 3.2.4. Leg 1 of the rosette trajectory was terminated at a planned stop at (27.393855 N, 111.364637 W), and Leg 2 was resumed at (27.460812 N, 111.527694 W); see Appendix A.2 for the schedule of bottle samples collected during Leg 2 presented in this manuscript. At the time of the transect, there were no

known hydrothermal sites present over the sampling trajectory, save for the northern ridge. Hydrothermal vents in the southern basin were located approximately 40 km further south from the transect starting location ([Teske et al., 2016]).

Modeling to Inform Transect Design

The selection of heights for the rosette and AUV *Sentry* was informed by a simple buoyancy model of expected plume characteristics on the ridge, and known operational constraints of AUV *Sentry* (i.e., an absolute floor and ceiling of operation above the bottom). Using an adapted plume crossflow model developed by [Tohidi and Kaye, 2016] (see Appendix A.5 for more detailed information) with a nominal current crossflow value of 0.1 m s^{-1} , vent temperature of 340°C , and estimated background seawater stratification as per [Speer and Rona, 1989], we hypothesized that a neutrally-buoyant layer may form between 1570 m and 1750 m. We selected the depths for the rosette (1600-1650 m) and AUV *Sentry* (1700-1750 m) given this information in order to target both the upper and lower estimated neutrally buoyant layer (NBL), respectively. We targeted the NBL to increase the likelihood of intersecting plume waters during the transect over a broad, multi-kilometer scope. This is in contrast with targeting the plume buoyant stem, which though significantly easier to distinguish from background seawater, may only have an expression on the order of several square meters.

Real-Time Data Feedback and Watchstanding

During the transect, data from the standard rosette sensors were available in near-real time at the watchstander station in the shipboard computer lab. This allowed watchstanders to monitor the depth of the rosette and relay requests to the winch operator on deck, and display the data on live-updating visualizers. AUV *Sentry* relayed occasional data packets up to 128 bytes in length at a rate of approximately 0.01 Hz. These data packets were subsequently graphed on a computer monitor that was linked to the *Sentry* network. A total of 600 messages with information about the standard science instruments on *Sentry*, and 583 messages with information from

the Pythia instrument were transferred during the transect.

3.3 Results

3.3.1 Methane Observations from Spectroscopic Instruments

Elevated methane was observed over a spatial scale of several kilometers, significantly rising as both AUV *Sentry* and the rosette approached the source of known hydrothermalism on the transect (Fig. 3-4). As both methane instruments used on this cruise were in active development, we report methane observations as normalized values from 0 to 1. We use a normalized value of 0.5 as a conservative threshold for classifying elevated methane measurements. Pythia, mounted on *Sentry*, reached and exceeded this threshold for elevated methane starting at approximately 3 km from the hydrothermal reference point at (27.407489 N, 111.389893 W); SAGE, flying nearly 50 m higher in the water column, reached this threshold starting 1.5 km away. For a less conservative threshold (0.3), these spatial detection points are reached 6.8 km and 2.2 km away, respectively. SAGE observed a sharp peak of methane just under 1 km from the reference source, with rapid decline of observable methane soon after. In contrast, Pythia reached a methane peak essentially at the 0km reference point, and shows a gradual decline in methane as *Sentry* descends into a graben just north of the hydrothermal ridge; the rosette was pulled from the water at the ridge. The difference in spatial detection patterns indicated by these instruments may be a function of both the different sensor modalities/sensitivities, and the natural structure of the neutrally-buoyant layer and the relative position of the two platforms within it.

3.3.2 Methane and Ammonium Observations with the Rosette

Ammonium is a microbial energy source and reduced compound that is produced by the hydrothermal vents at Guaymas Basin. It is expected that ammonium and methane behavior in the basin will behave similarly, providing a “check” on the methane trends we observe in methane bottle samples, and recorded by SAGE. Focus-

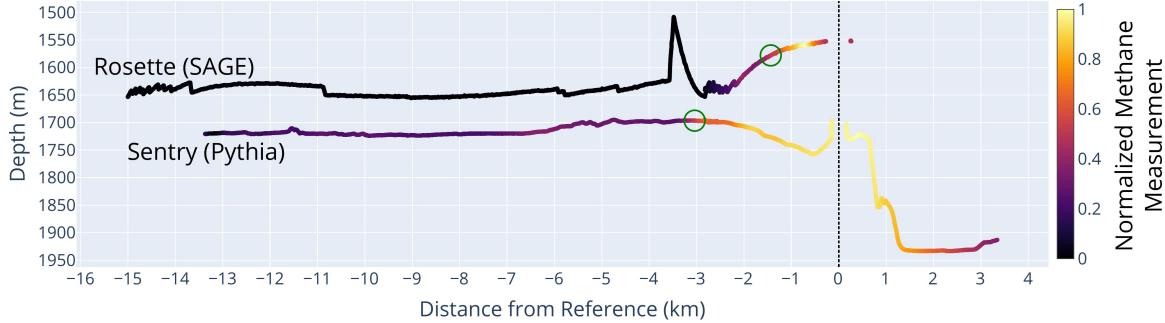


Figure 3-4: Normalized methane values observed with both SAGE (rosette) and Pythia (*Sentry*) over reference distance from (27.407489 N, 111.389893 W). The transect begins at the left of the plot and proceeds to the right. Strong methane anomalies, defined as points above a conservative threshold of 0.5 normalized values, are present starting 3 km from the reference source as observed by Pythia, and 1.5 km as observed by SAGE (open green circles).

ing primarily on Leg 2 of the rosette transect, we observed a correspondence between methane and ammonium elevation in the approach to the hydrothermal ridge (Fig. 3-5). Methane samples processed directly from Niskin bottles as outlined in Sec. 3.2.2 show a peak methane concentration of 3000-4000 nM (this range is associated with the extremes of calibrated extraction efficiencies valid for the equipment used), approximately 0.75 km from the hydrothermal reference point. Ammonium tracks closely with methane, at 3-4 times smaller concentration, reaching a peak of approximately 1000 nM.

Normalized methane observations by SAGE generally follow the trends shown by the bottle samples, similarly showing a spatial peak at 0.75 km. However, by its nature, SAGE yields a significantly more resolved signal; a small, secondary peak is observed by SAGE at 2 km from the reference point which is essentially missed by the bottle samples. Additionally, by virtue of operating continuously, there is no need for human interaction (unlike for processing bottle samples, which can require time-intensive *ex situ* analysis).

3.3.3 Turbidity

Turbidity is a commonly used indicator for detecting hydrothermalism from smoking vents; particulate matter produced by smoking vents can remain suspended in the

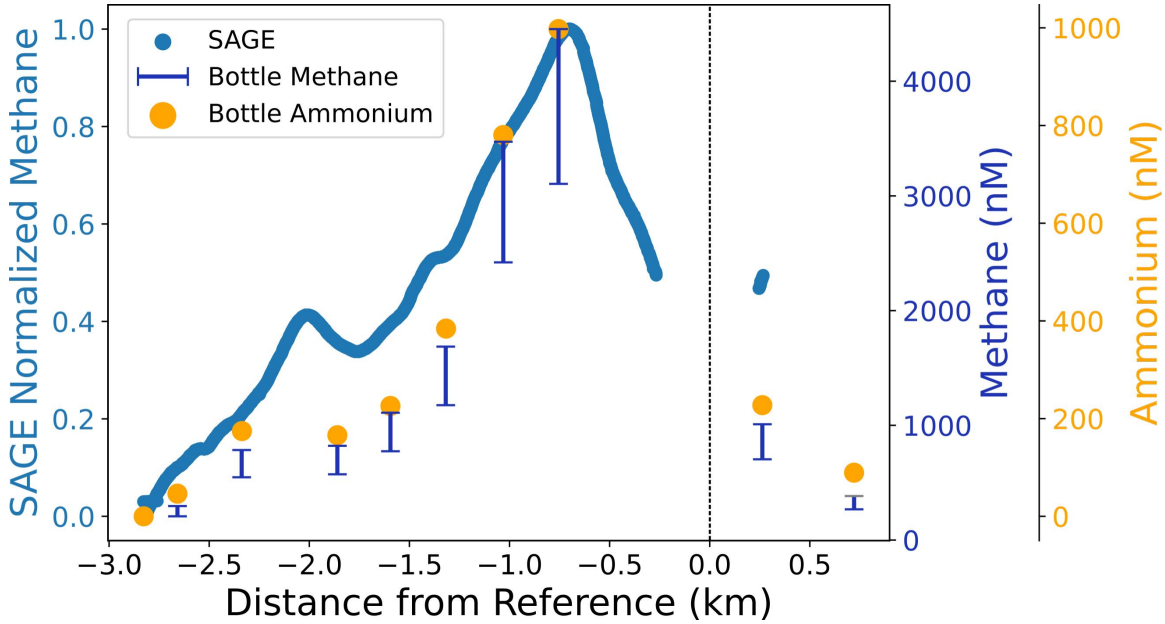


Figure 3-5: Normalized methane measurements by SAGE plotted with methane measurements taken from Niskin bottle samples (as measured by DGEU/GGA equipment) and ammonium measurements. Bottle methane measurements are reported as a range to reflect sensitivity of the measurement procedure to a calibrated extraction efficiency. All measurements trend towards a peak observation of methane and ammonium 0.75 km from the reference source. SAGE additionally observes a secondary peak approximately 2 km from the source, which is essentially missed by the bottle sample schedule.

neutrally buoyant layer, acting as a non-conservative tracer for hydrothermalism (e.g., [Feely et al., 1992]). In the Guaymas Basin, suspended particulates have been shown to be composed of metals like iron, aluminum, and manganese ([Scholz et al., 2019]) and are primarily mixed into bottom waters from hydrothermal activity. We report turbidity measurements as normalized values to make direct comparison between the platforms; in absolute terms, the transmissometer on the rosette reported beam attenuation values between 0-0.2 and the OBS on *Sentry* observed backscatter values between 0.08-0.14. The OBS on *Sentry* encountered an error from the beginning of the dive, potentially caused by a persistent air bubble, until approximately 4.5 km from the ridge reference point; we therefore do not report these early measurements.

We observed elevated turbidity (defined by a conservative threshold of 0.5 in the normalized data) with the transmissometer on the rosette starting approximately 2.2 km from the reference source and 3.3 km with the OBS on *Sentry* (Fig. 3-6).

Even with a less conservative threshold (0.3) these detection points only slightly improve to 2.5 km and 3.4 km respectively. With *Sentry*, we observe a rapid decline in turbidity within tens of meters west of the source reference (positive distance in Fig. 3-6). This may be indicative of the direction of prevailing crossflow (southeast) in the basin, which would directionally bend a buoyant plume stem and advect the neutrally buoyant layer.

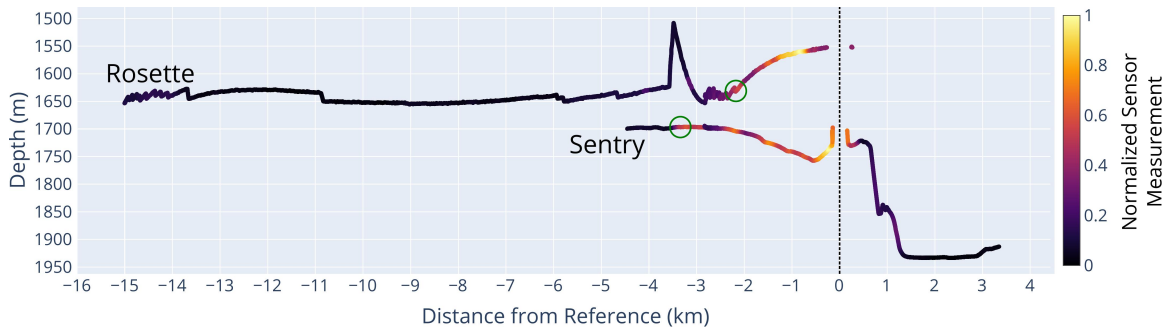


Figure 3-6: Turbidity observed as beam attenuation on the rosette transmissometer and optical backscatter on AUV *Sentry* instruments. *Sentry* encountered a sensor error until approximately 4.5 km from the ridge reference point. After this point, elevated turbidity is detectable throughout the dive, with significant elevations within 3.3 km east of the ridge reference point, dissipating within tens of meters to the west. Elevated turbidity is observed by the rosette 2.2 km from the ridge reference point to the east.

3.3.4 Oxidation Reduction Potential

AUV *Sentry* carries an ORP sensor; there was no comparable sensor on the rosette. ORP sensors are commonly used in hydrothermal plume hunting, and can be a strong indicator of recently emitted hydrothermal fluids. The derivative of ORP (noted here as dORPdt) is particularly used, in which negative dORPdt values typically indicate transition from background water into hydrothermal fluid. During the transect, only one significant dORPdt deviation was observed, within 200 m from the ridge reference point (Fig. 3-7).



Figure 3-7: The derivative of ORP observed by data collected on AUV *Sentry*. Negative slopes are indicative of entering hydrothermal fluids. Only one region of the transect demonstrated a significant reaction to ORP, within 200 m of the reference point.

3.3.5 Temperature, Salinity, and Oxygen

Temperature, salinity, and oxygen are expected to be weakly stratified in deep ocean waters, however fluids from hydrothermalism should register as anomalies when present. The magnitude of valid anomalies (i.e., anomalies that positively identify fluids impacted by hydrothermalism) can be exceedingly small; temperature at a vent can be hundreds of degrees Celsius, but anomalies in the water column on the spatial order of only 10 m can be measured as single degrees, and within a nonbuoyant plume on the order of hundreds of meters from the source, only register a few hundredths of a degree ([Yoerger et al., 2007]).

We compute temperature, salinity, and oxygen anomalies according to the process described in Sec. 3.2.3 and show the results in Fig. 3-8. Salinity anomalies, although apparently coherent, are reported within the empirical sensor noise for the CTD instruments on both the rosette and *Sentry*. Temperature anomalies on the scale of hundredths of a degree are observed throughout the transect, with two key regions of high temperature anomaly, one located 6-12 km from the reference source, and the other within 3 km of the source. Both the rosette and *Sentry* observe these regions; with *Sentry* observing the first anomaly in a narrower margin between 8-11 km from the reference source. The first region of positive temperature anomaly closely corresponds with marginally fresher water; whereas the region of higher temperature anomaly near the source is not consistently matched in temperature (the rosette

observes more salinity content, whereas *Sentry* observes neutral or slightly less salinity content). Oxygen is reported as nominal or slightly depleted within the regions of notable temperature and salinity anomaly.

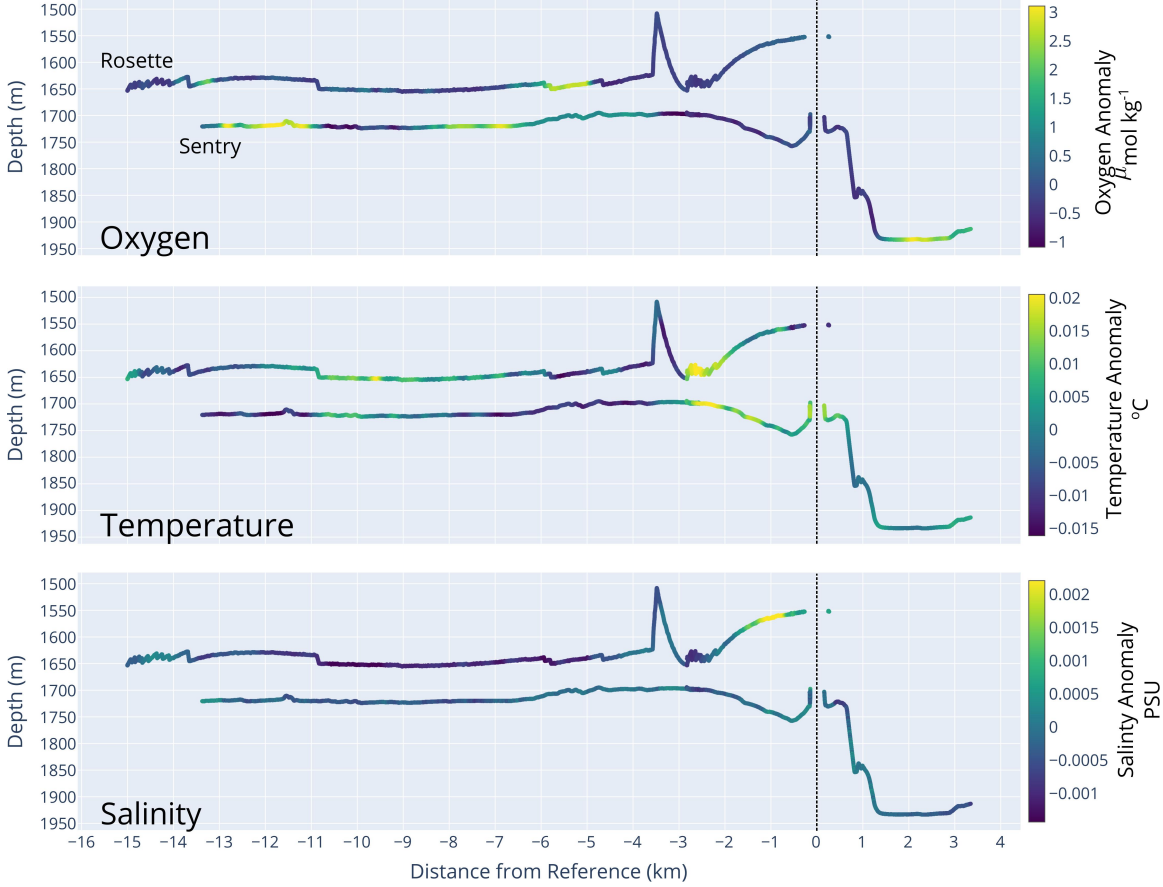


Figure 3-8: Depth-corrected oxygen, temperature, and salinity over reference distance. Two notable regions of high temperature deviation from expected temperature are observed between 6-12 km (rosette; 8-11 km by *Sentry*) and within 3 km of the reference source. The first region of temperature anomaly is closely matched with fresher salinity measurements; whereas salinity is measured as marginally higher near the reference source by the rosette CTD and nominal or lower by the *Sentry* CTD. In both regions, oxygen is nominal or slightly depleted, with regions of notably elevated oxygen at the boundary of these regions.

The first region of interest, far afield from the plume reference point, appears coherent and has similar detection qualities to the near-reference region; however, given the typical expectation of temperature dissipation from hydrothermal sources, it would be surprising if this first region were connected with hydrothermalism. The shape of the warm, slightly fresher and oxygen depleted intrusion (laterally broad

higher in the water column, and appearing to narrow based on the observations taken by the rosette and *Sentry* approximately 50 m offset in altitude) also does not follow expected patterns in a neutrally buoyant plume layer. Lack of significant methane and turbidity observations in this same region, as presented in Sec. 3.3.1 and Sec. 3.3.3 respectively, additionally casts doubt on hydrothermalism as a driver for this anomaly. Water mass mixing between the bottom waters, largely sourced from Pacific Deep Waters and the Pacific Intermediate Waters ([Bray, 1988]) may be an alternative explanation, but is out of scope for this paper to investigate.

3.4 Discussion

3.4.1 Sensor Cross-Correlations

Successfully detecting hydrothermalism in the deep ocean is a significant challenge, and detection may be most effective using a combination and corroboration of anomalies across multiple sensor inputs (e.g., [Jakuba, 2007]). Here, we examine the cross-correlation between sensors mounted on each of the platforms. Both a global and rolling Pearson correlation coefficient was computed, showing respectively overall correlation trends, and situation dependent correlation.

Fig. 3-9 shows the global correlation among sensors mounted on the rosette individually over Leg 1 and Leg 2, in addition to sensors mounted on *Sentry*. In the absence of significant geochemical features in a target environment, it is expected that no or only weak correlation will be computed globally, as individual sensor noise (which is independent) will dominate the computation; when geochemical structure is present in the environment, it is expected that weak to strong global correlation will be computed as the environment is imposing a (shared) signal across at least a subset of sensors. This is well illustrated by the cross-correlation matrices for the rosette legs, with global coefficients for Leg 1 reporting no correlation between sensors save for a slightly negative correlation between temperature and oxygen, and for Leg 2 reporting weak to strong correlations between all sensors, with notably strong

positive correlation between turbidity and methane. Interestingly, in Leg 2 a negative correlation is reported between temperature and methane, and a positive correlation is measured between methane and oxygen measurements. This runs directly counter to expectations; and also counter with the relationships observed by *Sentry* which marks relationships between methane and temperature as positively correlated, and between methane and oxygen as negatively correlated.

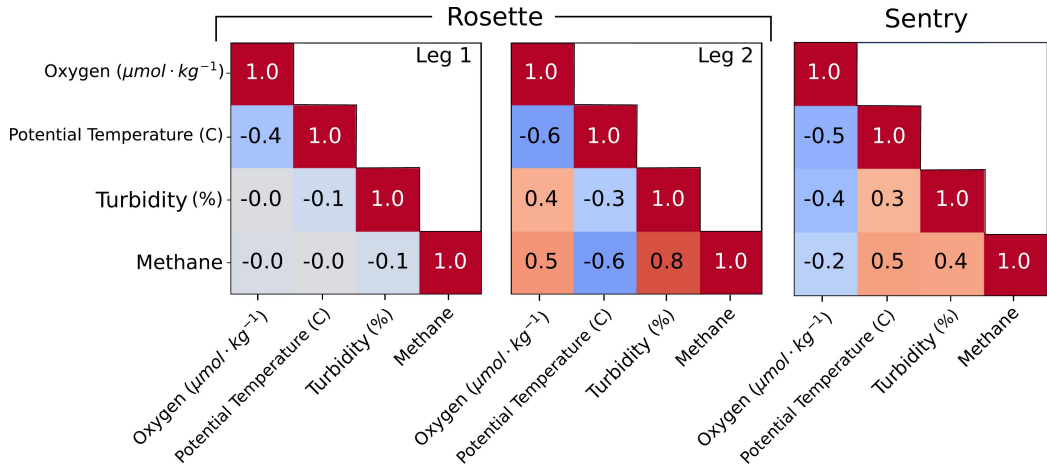


Figure 3-9: Global Pearson correlation coefficient between sensors mounted on the rosette and *Sentry*. Correlation differences between Leg 1 (far from the reference point) and Leg 2 (near the reference point) are indicative of different sensor correlation behaviors with respect to ambient seawater conditions and hydrothermal fluid interception. *Sentry* correlation coefficients reflect an expected relationship between temperature and methane (positive), methane and oxygen (negative), and turbidity and methane (positive) that may be stereotypically associated with hydrothermal fluids. In contrast, the Leg 2 rosette correlation factors do not meet this expectation, despite showing strong overall correlative structure.

The difference between correlative behaviors between the rosette legs, and also between the platforms generally, motivates a finer study of correlation. Fig. 3-10 shows a rolling correlation coefficient computed over a window of 30 minutes for the rosette. Computing local cross-correlations with respect to time, rather than distance, is mathematically more sound, and also aligns directly with how cross-correlative monitoring may be used during live exploration missions. With respect to the rosette, we observe that in Leg 1, nominal correlation is weak or non-existent between most sensors, with exception for oxygen and temperature. We can additionally see that the correlative “micro-structure” of the local window shows regions of possible interest that are

greater than nominal – for instance, measurements taken between 03:00-05:00 show a coherent region of negative correlation between temperature and turbidity, and positive correlation between temperature and oxygen. Similarly, around 02:00 a region of strong positive correlation between oxygen and temperature is observed. In Leg 2, we see overall more strong, pronounced correlations between sensors, with a distinct period centered in the hour around 10:00 in which correlation between temperature and methane, temperature and turbidity, oxygen and methane, and oxygen and turbidity appear to “flip” compared to the periods of time directly before and after this period, potentially indicating a significant anomalous feature. This time period is well aligned with the spatial proximity of the rosette with the reference source.

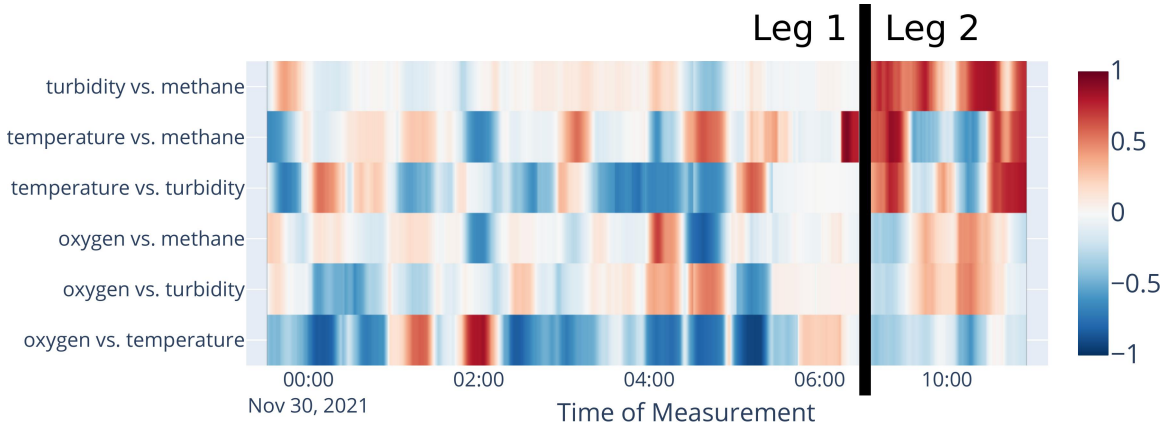


Figure 3-10: Local (rolling) Pearson correlation coefficients between sensors mounted on the rosette over 30 minute windows.

Local correlation trends during the *Sentry* transect are reported in Fig. 3-11, and show an intense relationship between oxygen and temperature throughout the dive, with most regions reporting a strong negative correlation, both with two regions showing positive correlation between 07:00-08:00 and again at 11:00. This strong relationship is also reflected in the relationships of temperature and oxygen with methane, being nearly correlative mirrors with respect to methane. During periods in which the turbidity sensor was operational, a gradual correlative “flip” and intensity increase around the 11:00 sampling time may indicate a structured water mass. This time agrees with the spatial proximity of *Sentry* with the reference source.

Correlation alone is not sufficient evidence for the presence of hydrothermal flu-

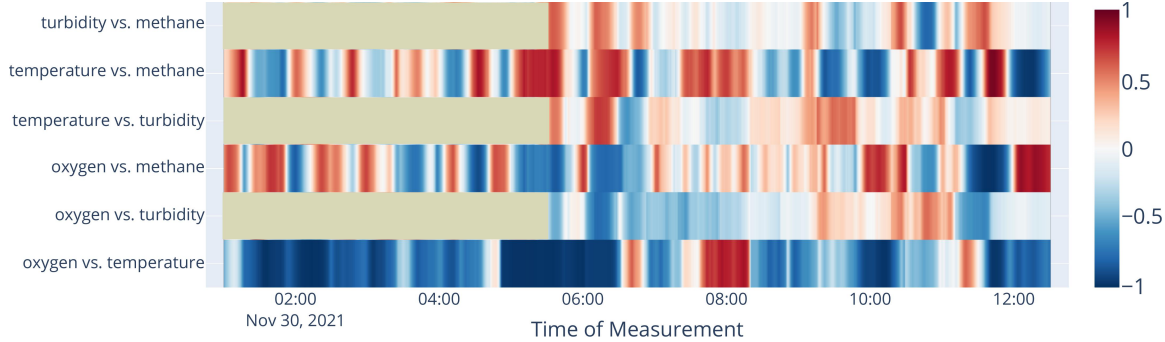


Figure 3-11: Local (rolling) Pearson correlation coefficient between sensors mounted on AUV *Sentry* over 30 minute windows.

ids. For instance, some of the coherent regions of positive or negative correlation with methane any time during Leg 1, or early in the *Sentry* transect, are misleading, as the overall methane content of the water was exceedingly small or essentially background. Rolling correlations, coupled with absolute thresholds as reported in this results section, may together be useful tools for indicating transition into new water masses, their absolute properties of which could be used to more closely classify the types of water masses. This correlative study also demonstrates that correlations in expectation (e.g., temperature and methane being positively correlated in hydrothermal fluid) may be reductive assumptions of the complexities of plume evolution within a water column, supporting similar findings by, e.g., [Cowen et al., 2002]. For instance, aging plume waters in the neutrally buoyant layer may long have settled to a temperature indistinguishable from background, but still be particulate and possibly gas rich. This motivates additional study of the “classes” of hydrothermal fluids and their classifying characteristics, which could in turn be used to support studies of microbial evolution and nutrient consumption in plume fluids, or sediment and particulate transport modeling.

3.4.2 Hydrothermalism Detection via Time-Series Regimes

As indicated by Sec. 3.4.1, changes in correlative *structure* may be a more useful signal than absolute correlation alone. This notion can be codified as regime changes, which detect inflection points in which a series of observations collected in time may

change in typical value, oscillation frequency, or pattern. Here, we compute regime changes using a 30 minute detection window using the `ruptures` Python library and a radial basis function detection kernel, and report regimes using alternating red and blue color blocks in the included figures.

In Fig. 3-12 we show uniquely identified regimes across the entire rosette transect over multiple sensors. We observe that the water-mixing anomaly that occurs early in the transect (Sec. 3.3.5) appears to be detected as regime changes in potential temperature, oxygen, and even a correspondence in lowered beam attenuation. Similarly, regime changes in turbidity and methane are early indicators of significant elevation of both of these factors as the rosette intersects with hydrothermal fluids. Interestingly, a regime change in oxygen and temperature is evident immediately following the first small peak in methane and turbidity. These peaks, in addition to these regime changes, may together be indicative of mixing plume sources from other hydrothermal vents located along the ridge (that must travel further than fluids from our reference point) or the mixing of ageing plume waters with more recently emitted fluids.

With instruments mounted on *Sentry*, in Fig. 3-13 we see clear “steps” of methane observed by Pythia each marked as a regime. Some of these steps are nearly coincident with regime changes in turbidity, temperature, and oxygen (particularly the steps at 06:30 and 09:30).

Regimes can be mathematically identified in streaming data, making this a potentially useful method to adopt for real-time hydrothermalism discovery. Coupled with absolute measurements by sensing instruments and rolling correlative structure, identifying water masses across multiple data streams can be done live from streaming data on the ship, or computed/estimated directly onboard an AUV computer and reported back to watchstanders remotely under data-limited transmission protocols (e.g., acoustic pings).

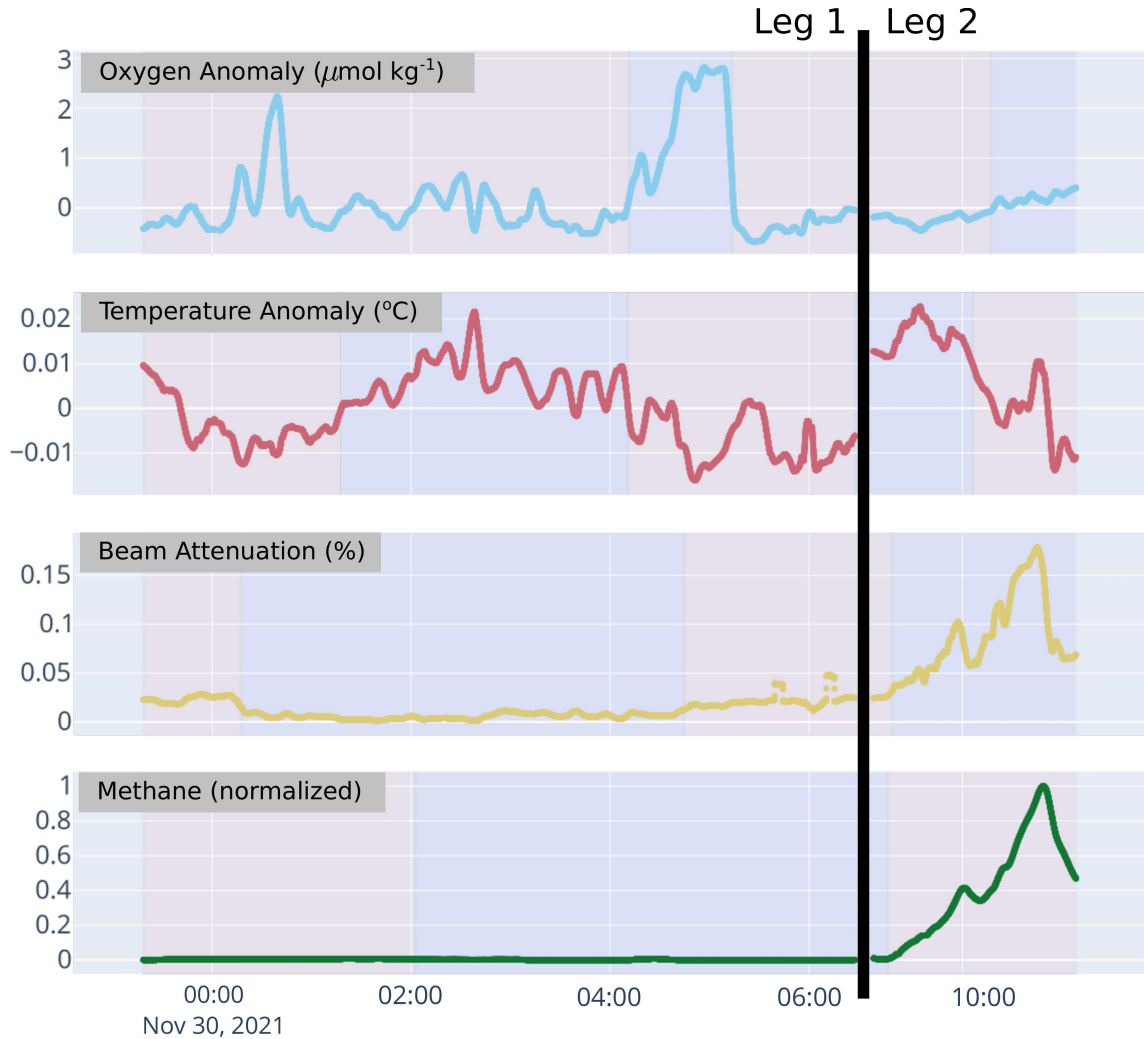


Figure 3-12: Regimes, indicated as alternating blue and red regions, detected during the rosette transect with a 30 minute detection window.

3.4.3 Methane in Deep Sea Exploration

AUV and sensor deployments during expedition RR2107 served as an initial proving ground for the SAGE and Pythia *in situ* methane instruments for deep sea exploration, and the utility of methane as a potential tracer for hydrothermalism discovery. We showed that, during this transect, both instruments observed significantly elevated methane over a span of several kilometers from a known hydrothermal source in Guaymas Basin. Methane proved to be a strong predictor for hydrothermalism that was not easily confounded by physical oceanographic events (e.g., mixing), giving it an advantage over oxygen, temperature, and salinity. Indeed, in this trial, each

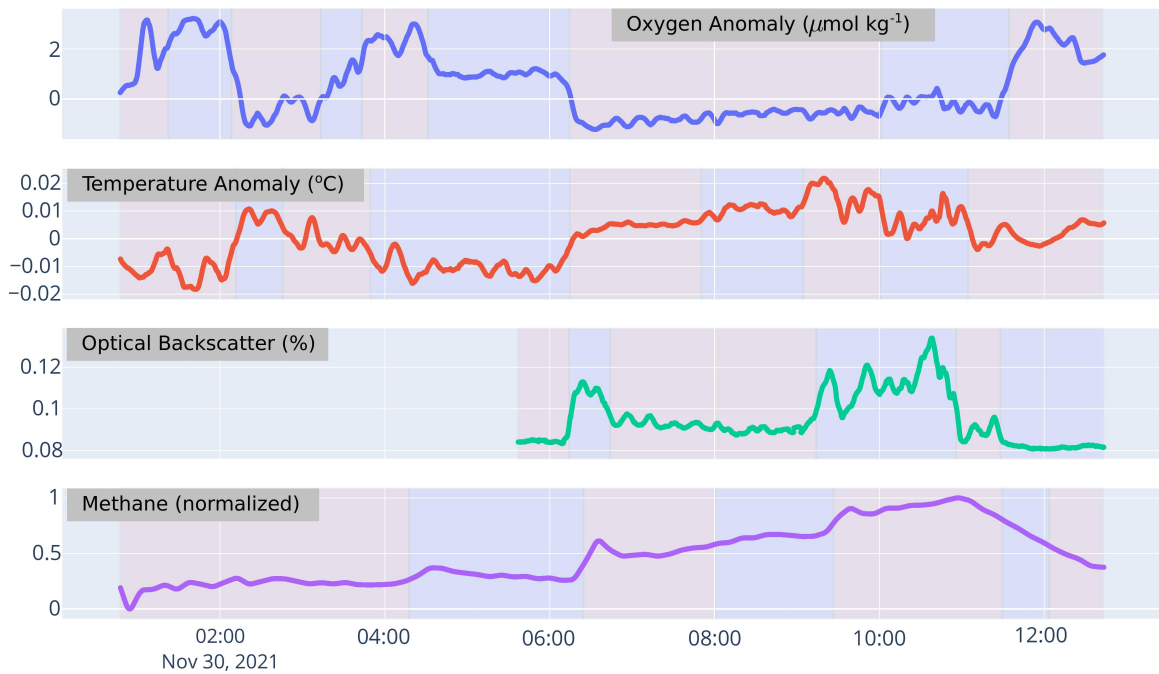


Figure 3-13: Regimes, indicated as alternating blue and red regions, detected during the AUV *Sentry* transect with a 30 minute detection window.

of the oxygen, temperature, and salinity instruments were impacted by an unknown physical feature not driven by hydrothermalism, but registered as similar scales of expected anomaly. Methane was also shown to be more expressive than ORP, which only registered a possible anomaly long after significant methane measurements were observed. Turbidity was a similarly useful and expressive feature of hydrothermalism in this basin, with similar detection scales to methane during this transect. Notably, for less strict detection criteria (i.e., thresholds) on detection, methane significantly outperformed turbidity in terms of detection scale (positive identification up to 6.8 km away, in contrast to 3.4 km for turbidity). Turbidity and methane together make for a strong pairing for hydrothermalism discovery. While neither one alone is a "universal" proxy for hydrothermal activity—not all hydrothermalism of interest produces particulate heavy smoke (i.e., diffuse flow fields) nor do all vents produce significantly elevated methane—they are complementary indicators which can assist in deep sea exploration for anomalous water masses derived from hydrothermalism.

Collecting high resolution measurements of methane during this transect highlighted the rich structure of dissolved gasses in a neutrally buoyant plume layer over

multiple kilometers, with multiple peak detections being possibly indicative of mixing novel and ageing hydrothermal fluids, the contribution of multiple sources of hydrothermalism, or complicated internal mixing causing spatiotemporal multimodal distributions of dissolved gas “pockets” throughout the layer. Bottle samples collected on the cruise verified the presence and general trend of methane observed by the instruments, but failed to resolve several features that may be of scientific interest. This motivates the use of *in situ* methane sensors for future studies of hydrothermal fluids in the water column.

3.4.4 Enabling Better Decision-Making for Hydrothermalism Discovery

Enabling the interpretation of real-time sensor data and adapting scientific missions accordingly are critical future skills for scientific expeditions and exploration in the deep sea. In preparation for this transect, we utilized a simple physical model to inform the design of the trajectory and monitored progress with live data displays for both the rosette and AUV *Sentry*. While real-time data display for rosettes is now considered standard for oceanographic research, streaming capabilities of scientific data from autonomous platforms like *Sentry* is a relatively new capability. This display infrastructure enabled the science team to make note of the OBS sensor error on *Sentry* while performing the transect, caught a power and logging failure of the Pythia logger upon deployment (which, if left unresolved, would have meant an absence of all methane data associated with *Sentry* for this analysis), and allowed real-time control and decision-making about the rosette positioning and bottle firing possible. While data presented here was analyzed after the mission, several of these analyses, including rolling correlation and regime detection, could be performed from streaming observations. As a whole, the techniques in this paper present an opportunity for advancing technical infrastructure on a research vessel in order to enhance decision-making capabilities of the science party and engineering teams, both logistically to better diagnose instrument operation *in situ* and scientifically to enhance

data collection.

Real-time data collection and processing could have further implications for embodied intelligence as a tool for scientific expeditions. Using models, inference methods, and streaming data, autonomous agents like AUV *Sentry* could be made capable of performing adaptive decision-making for sample collection. Hydrothermalism discovery has long been a motivating use case for intelligent autonomy at sea (e.g., [Yoerger et al., 2007, Jakuba, 2007, Branch et al., 2020, Wang et al., 2020]). This transect experiment demonstrates the utility of simple models for tractable, intelligent planning, motivates the possibility of using methane as an additional, reliable data source for performing autonomous behaviors (e.g., adaptive sampling, tracking), and presents the opportunity to embed simple analytical methods for classifying hydrothermal fluids from sensor streams. Being able to not only estimate and map the source of hydrothermal plumes, but to also chart the evolving nature of fluids in the mid-water, would enable an advancement of scientific inquiries that could be pursued with respect to hydrothermalism in the deep ocean. Such queries include the detailed structure of multiple-source plume collision, directly measuring *in situ* the 4D structure of mixing in neutrally buoyant plumes and buoyant plume stems, assessing biological activity supported by plume fluids, tracing the fate of dissolved gasses, and more. We have shown that detection of hydrothermal sources is possible on the scale of several kilometers even in this relatively small basin, and have taken some initial steps to demonstrate core data infrastructure that can improve human decision-making in hydrothermalism discovery; future work and engagement will be focused on advancing these tools to enable the next generation of scientific inquiry in the deep ocean.

3.5 Interpreting Point Observations of Hydrothermal Fluids

PSEUDO-SENSOR

3.6 Leveraging Sensors of Opportunity

PIV, Tiltmeters, Observatories, Now-casts, Forecasts

3.7 Summary

Chapter 4

Predicting: Representing Belief and Simulating Uncertain Dynamics

4.1 General Models: GPs

4.2 Embedded Physical Models: PHUMES

4.3 Physically-Informed Learned Models: PIKL

4.4 Performance in Hydrothermal Domains

4.5 Summary

Chapter 5

Planning: Adaptive Sampling in Spatiotemporal Fields

5.1 Underway Autonomy: PLUMES

5.2 Deployment-by-Deployment Autonomy: PHOR-
TEX

5.3 Field Results in GB

5.4 Summary

Chapter 6

Discussion

6.1 Generalizing to Other Domains

6.2 Open Challenges

6.3 Embedding Autonomy Engineers into Science Teams

6.4 Robotics in Expeditionary Science

Chapter 7

Looking Forward

This is the conclusion section.

Appendix A

Perceiving: Supplemental Information

A.1 Method for Methane Measurement from Niskin Bottles

A Los Gatos Research (LGR) Dissolved Gas Extraction Unit (DGEU) and Greenhouse Gas Analyzer (GGA) were used to process water collected by Niskin bottle samples during the transect, and report methane concentration estimates to be compared to the *in situ* observation of normalized methane by SAGE mounted on the rosette. Measurements of methane made by the GGA are reported as the stabilized parts per million (ppm) reading provided by the instrument after consuming 3-5 L of seawater from each Niskin bottle, and are converted to nanomolar (nM) values by first computing the partial pressure of methane, and then computing molarity by estimating the solubility constant of methane using coincident measurements of salinity and temperature of the seawater at time of bottle sample collection as measured by the rosette CTD. The conversion from partial pressure to molarity is done using the `gasex` Python library, publicly hosted at <https://github.com/boom-lab/gasex-python>.

To transform GGA measurements in ppm to partial pressure, the DGEU cell pressure is used, such that $\text{ppm} \times \text{cell pressure} = \text{partial pressure}$. Additionally, gas

extraction inefficiency is taken into consideration at this step; the DGEU does not perfectly extract gas across the membrane during sampling. Extraction efficiency is used to scale the GGA measurement of methane prior to computing the partial pressure estimate by

$$\left[\frac{x_{obs} - x_{ref}}{\lambda_{eff}} + x_{ref} \right] \frac{p_{cell}}{1000} = x_{pp} \quad (\text{A.1})$$

where x_{obs} is the ppm measurement made by the GGA, x_{ref} is a methane reference value (the atmospheric concentration of methane, typically between 1.86-1.99 ppm), λ_{eff} is the extraction efficiency, p_{cell} is the cell pressure in millibar, and x_{pp} is the estimated partial pressure value, in μatm .

The extraction efficiency used in this manuscript was estimated by laboratory calibrations to be between 2.3-3.3%, consistent across different water temperatures and different test tank concentrations. In the laboratory calibration procedure, methane was bubbled in a temperature-controlled tank which was stirred before two discrete samples were taken using 60 mL syringes filled with 40 mL of water, and 20 mL of pure nitrogen gas. A DGEU, connected to the GGA, was then used to take water from the target tank, and ppm measurements by the GGA were recorded when measurements stabilized; this was done with two different DGEUs, which we label A and B. To estimate “ground truth” partial pressure of methane in the tank, the syringe samples were shaken for 2 minutes to extract the dissolved gas content, and the water drained. The samples were then processed within 24 hours on a gas chromatography instrument (Shimadzu GC-14B), run alongside a set of standards processed every 5 minutes. The measurements from the processed syringes (DGEU influent) were used as x_{pp} in Eq. A.1, the GGA observations as x_{obs} , the value 1.99 ppm used as x_{ref} , and 495 mbar as p_{cell} . The relevant data from these calibrations is available in Tab. A.1. DGEU A was the instrument used in the transect field mission as presented in this manuscript.

DGEU	Temperature (C)	Influent (μatm)	GGA Methane (ppm)	Efficiency
A	4.7	299.13	21.82	3.29%
A	4.7	512.03	6.44	0.4%
A	4.7	588.25	41.04	3.29%
B	4.7	299.13	17.77	2.62%
B	4.7	512.03	25.68	2.29%
B	4.7	588.25	30.09	2.37%
A	9.9	267.14	17.02	2.80%
A	9.9	403.45	27.84	3.18%
A	9.9	856.89	55.77	3.11%
B	9.9	267.14	12.72	2.00%
B	9.9	403.45	18.63	2.05%
B	9.9	856.89	36.99	2.02%
A	14.8	18.64	2.78	2.22%
A	14.8	1549.18	101.26	3.17%
A	14.8	1640.81	100.41	2.97%
B	14.8	18.64	2.63	1.80%
B	14.8	1549.18	78.93	2.46%
B	14.8	1640.81	68.43	2.01%

Table A.1: Results of DGEU extraction efficiency calibration experiments.

A.2 Leg 2 Niskin Bottle Sample Schedule and Measurements

This manuscript presents methane and ammonium measurements collected by Niskin bottles during Leg 2 of the rosette trajectory. Table A.2 provides the schedule of Niskin bottle firing performed during Leg 2, and Table A.3 provides all data associated with those bottles collected and presented in Chapter 3 of this thesis. The range of methane nM values is provided by converting GGA methane ppm measurements as described in Sec. A.1 for the conservative range of valid DGEU extraction efficiency values.

Bottle	Time	Location	Depth (m)
1	2021-11-30 09:10:03	27.3951N 111.3649W	1648.62
3	2021-11-30 09:30:03	27.3956N 111.3665W	1625.67
5	2021-11-30 09:47:01	27.3967N 111.3696W	1639.25
7	2021-11-30 09:47:05	27.3967N 111.3696W	1639.05
9	2021-11-30 10:07:00	27.3985N 111.3740W	1598.32
11	2021-11-30 10:17:02	27.2994N 111.3765W	1580.5
13	2021-11-30 10:27:01	27.4005N 111.3791W	1568.27
15	2021-11-30 10:27:04	27.4005N 111.3791W	1568
17	2021-11-30 10:37:20	27.4016N 111.2818W	1558.64
19	2021-11-30 10:46:59	27.4027N 111.3845W	1553.92
21	2021-11-30 11:07:05	27.4051N 111.3900W	1547
23	2021-11-30 11:33:00	27.4082N 111.3971W	1545.4

Table A.2: Schedule of bottle samples during Leg 2 of rosette trajectory.

Bottle	CH ₄ (ppm)	CH ₄ (nM)	NH ₄ ⁺ (nM)	Temp. (C)	Salinity (PSU)
1	–	–	0.00	2.8334	34.6104
3	9.29	207-296	46.35	2.8578	35.6095
5	21.6	547-785	–	2.8458	34.6107
7	–	–	174.48	2.8461	34.6108
9	22.54	573-821	165.99	2.8659	34.6101
11	29.82	774-1110	225.87	2.8719	34.6096
13	44.36	1176-1686	–	2.8734	34.6099
15	–	–	384.28	2.8733	34.6098
17	89.45	2421-3473	780.53	2.8849	34.6105
19	114.27	3105-4454	997.45	2.8968	34.6111
21	27.29	704-1009	227.54	2.8835	34.6087
23	11.5	268-384	89.29	2.8964	34.6075

Table A.3: Geochemical measurements associated with the schedule of bottle samples during Leg 2 of rosette trajectory. Note that methane expressed in nM is computed using coincident temperature and salinity measurements during the transect as measured by rosette CTD, and extraction inefficiency of the DGEU is compensated for as described in Sec. A.1.

A.3 Normalized Pythia Calibration

The Pythia instrument provides a significantly nonlinear output reference value when measuring methane. We correct for this nonlinearity using a reference curve com-

puted in the laboratory before normalizing the measurements as reported in this manuscript. The reference curve was created using a temperature-fixed (3°C) tank and closed equilibration chamber, in which methane standards were bubbled until fully equilibrated before being measured by the instrument. Stable measurements by Pythia (which has a response time of approximately 35 minutes) were then recorded at different chamber concentrations. The calibration curve that results is a piece-wise linear function, shown in Fig. A-1.

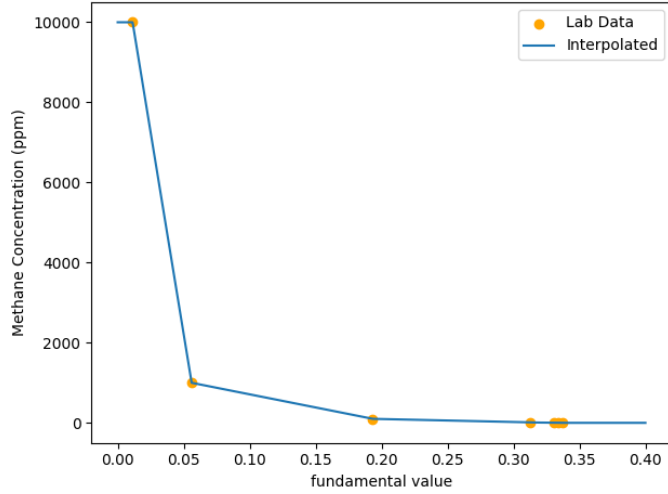


Figure A-1: Fitted calibration curve for measurements of methane observed by Pythia.

Compensation of Pythia’s time response was also performed on post-calibrated data using the methodology described in [Miloshevich et al., 2004] with a smoothing window of 5 minutes, and subsampling at a quarter of the time delay window. This methodology is sensitive to noise in the signal, which motivates the extreme subsampling that is performed. Fig. A-2 shows the effect of smoothing, time-correction, and conversion on the direct signal recorded by Pythia before normalization.

A.4 Depth-Correction

Temperature, salinity, and oxygen are expected to be weakly stratified in the deep ocean. To remove these effects from data collected by AUV Sentry and the rosette,

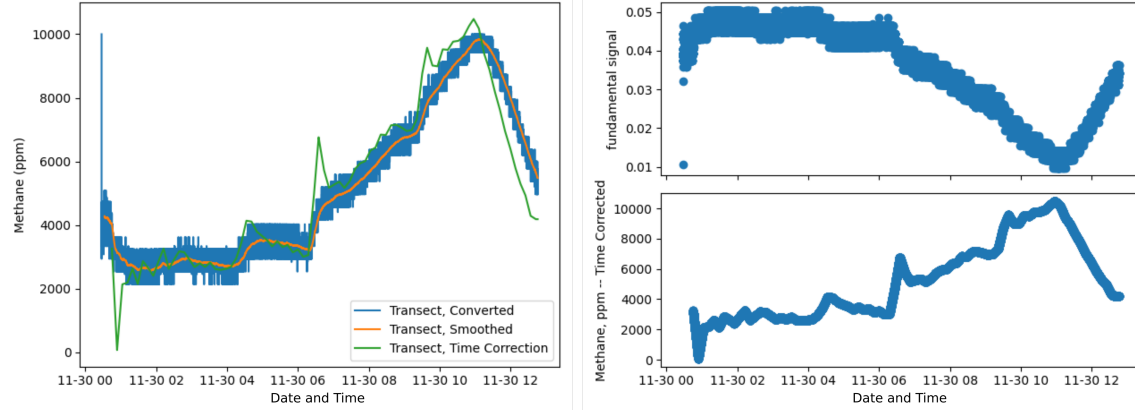


Figure A-2: Calibration curve, smoothing, and time correction applied to Pythia observations during the transect, before reported normalization in the manuscript.

we fit a line to the average observations collected within binned 20 m intervals of observed depth for each platform separately. Separately computing the correction for each instrument additionally controls for small discrepancies in calibration between the platforms. Fig. A-3 compares these lines with the observations collected.

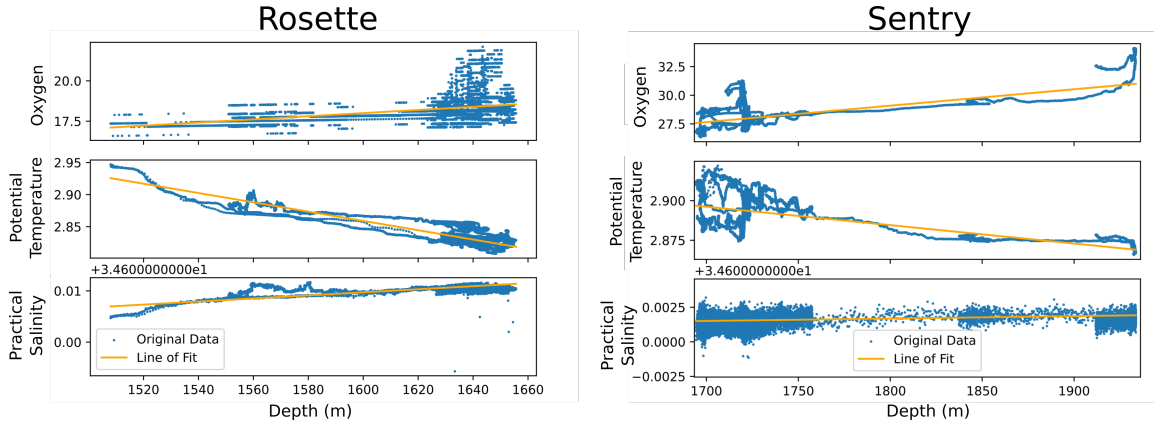


Figure A-3: Linear functions are fit to data collected for oxygen, temperature, and salinity instruments on each platform separately. A residual value is then computed for each observation.

A.5 Description of Plume Model for Transect Design

We adapted an idealized buoyant bent-plume model proposed by [Tohidi and Kaye, 2016] for atmospheric bent plumes in a weakly stratified fluid in order to inform at

what heights to deploy AUV Sentry and the rosette during the transect. We rewrite the system of equations provided in [Tohidi and Kaye, 2016] as follows:

$$E = \alpha \left| \frac{M}{Q} - u \cos(\theta) \right| + \beta |u \sin(\theta)| \quad (\text{A.2})$$

$$\frac{dQ}{ds} = QE \sqrt{\frac{2(1 + \lambda^2)}{M\lambda}} \quad (\text{A.3})$$

$$\frac{dM}{ds} = u \cos(\theta) \frac{dQ}{ds} + \frac{FQ}{M} \sin(\theta) \quad (\text{A.4})$$

$$\frac{d\theta}{ds} = \left(\frac{FQ}{M} \cos(\theta) - u \sin(\theta) \frac{dQ}{ds} \right) \frac{1}{M} \quad (\text{A.5})$$

$$\frac{dF}{ds} = -QN^2 \sin(\theta) \quad (\text{A.6})$$

$$\frac{dX}{ds} = \cos(\theta) \quad (\text{A.7})$$

$$\frac{dZ}{ds} = \sin(\theta) \quad (\text{A.8})$$

where E is a mixing entrainment coefficient which considers both vertical and horizontal mixing and is weighted by parameters α and β , u is the crossflow velocity which can be a function of depth and time, λ is a parameter which modifies the ellipse which describes the plume envelope, Q is specific volume flux, M is specific momentum flux, F is specific buoyancy flux, θ is plume centerline trajectory angle, s is the plume centerline trajectory, X is distance along a coordinate axis aligned with the plume centerline, Z is height with respect to plume source along a vertical axis, and N^2 is the Brunt-Väisälä frequency, computed with respect to the density gradient at the reference depths of the source and plume height.

The system of equations essentially yields a “snapshot” of a plume envelope at some moment in time. For time-varying crossflows, multiple snapshots can be computed for different moments in time (different crossflow orientations and magnitudes) and chained together in a common coordinate reference system in order to track a plume trajectory. For the purposes of determining which heights to deploy AUV Sentry and

the rosette for the transect, we compute a prototypical envelope and use the estimated bent nonbuoyant plume height to set the transect depths/altitudes.

The initial conditions for solving this system of ordinary differential equations are set via estimates of vent characteristics including exit velocity, temperature, salinity, and area. Specifically:

$$Q_o = \lambda V_v \frac{A_v}{\pi} \quad (\text{A.9})$$

$$M_o = Q_o V_v \quad (\text{A.10})$$

$$F_o = -g 10^{-4} (T_v - T_z) Q_o \quad (\text{A.11})$$

$$\theta_o = \frac{\pi}{2} \quad (\text{A.12})$$

where V_v is exit velocity at the vent orifice, A_v is the vent orifice area, T_v is the temperature at the orifice area, and T_z is the expected temperature of ambient seawater at the estimated vent depth. Note that initial buoyancy flux is primarily driven by temperature changes, as we anticipate this to be the major driver of density gradients at our measurement scale. Expected salinity gradients could be similarly considered.

Estimated vent characteristics and crossflow were selected based on empirical observations of the deep sea vents located along the northern Guaymas Basin ridge and observations of current magnitude collected by a current tiltmeter deployed by ROV Jason during several days of the research cruise. Table A.4 lists the settings for planning the transect selected for these characteristics. Background salinity and temperature profiles were computed according to standard Pacific Ocean temperature and salinity functions as described in [Speer and Rona, 1989]; additionally the equation of state for computing density profile from salinity and temperature measurements was used also as defined in [Speer and Rona, 1989]. The prototypical plume is computed with a source located at 1850 m depth.

The prototypical plume envelope computed in this manner estimates a nonbuoyant plume depth between 1570-1750 m (Fig. A-4). AUV Sentry is altitude limited in order to keep a fix on the ocean floor for navigation; it is set to its maximum altitude

Parameter	Assignment	Description
λ	1.0	Ratio of elliptical axes of the plume envelope
V_v	0.58 m s^{-1}	Exit velocity of fluids at vent orifice
A_v	0.82 m^2	Area of vent orifice
T_v	340°C	Temperature of fluids at vent orifice
α	0.15	Longitudinal shear-driven mixing coefficient
β	0.19	Transverse shear-driven mixing coefficient
u	0.1 m s^{-1}	Magnitude of crossflow

Table A.4: Parameter, vent characteristics, and ambient crossflow setting used for transect design.

of 120 m in order to intersect with the bottom of the estimated nonbuoyant layer; this corresponds to a depth of approximately 1700 m throughout the basin. The rosette can be arbitrarily fixed to a height, but so as not to interfere with AUV Sentry operations and to sample a different point in the estimated nonbuoyant layer, a depth of 1650-1600 m was targeted.

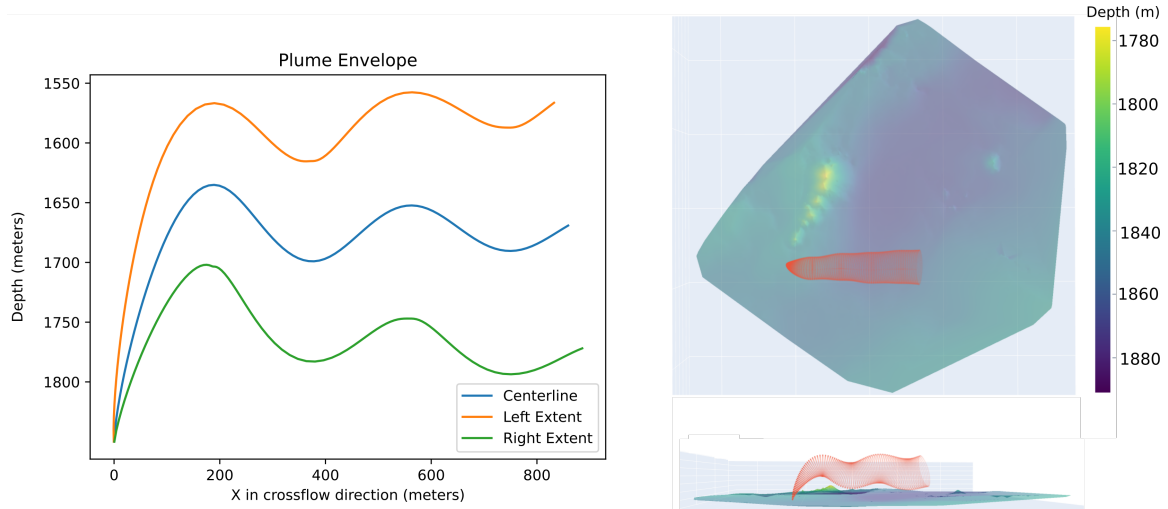


Figure A-4: A prototypical plume estimate according to the modified buoyant plume model in crossflow. The same envelope is plotted with respect to absolute depth (with a source located at 1850 m) on the left, and illustratively in the context of the hydrothermal ridge on the right.

Bibliography

- Beaulieu, S. E., Baker, E. T., and German, C. R. (2015). Where are the undiscovered hydrothermal vents on oceanic spreading ridges? *Deep Sea Research Part II: Topical Studies in Oceanography*, 121:202–212.
- Bell, J. B., Woulls, C., and Oevelen, D. v. (2017). Hydrothermal activity, functional diversity and chemoautotrophy are major drivers of seafloor carbon cycling. *Scientific reports*, 7(1):1–13.
- Bennett, S. A., Coleman, M., Huber, J. A., Reddington, E., Kinsey, J. C., McIntyre, C., Seewald, J. S., and German, C. R. (2013). Trophic regions of a hydrothermal plume dispersing away from an ultramafic-hosted vent-system: Von Damm vent-site, Mid-Cayman Rise. *Geochemistry, Geophysics, Geosystems*, 14(2):317–327.
- Branch, A., McMahon, J., Xu, G., Jakuba, M. V., German, C. R., Chien, S., Kinsey, J. C., Bowen, A. D., Hand, K. P., and Seewald, J. S. (2020). Demonstration of autonomous nested search for local maxima using an unmanned underwater vehicle. In *2020 IEEE International Conference on Robotics and Automation (ICRA)*, pages 1888–1895. IEEE.
- Bray, N. (1988). Water mass formation in the Gulf of California. *Journal of Geophysical Research: Oceans*, 93(C8):9223–9240.
- Camilli, R., Reddy, C. M., Yoerger, D. R., Van Mooy, B. A., Jakuba, M. V., Kinsey, J. C., McIntyre, C. P., Sylva, S. P., and Maloney, J. V. (2010). Tracking hydrocarbon plume transport and biodegradation at deepwater horizon. *Science*, 330(6001):201–204.
- Chin, C. S., Coale, K. H., Elrod, V. A., Johnson, K. S., Massoth, G. J., and Baker, E. T. (1994). In situ observations of dissolved iron and manganese in hydrothermal vent plumes, Juan de Fuca ridge. *Journal of Geophysical Research: Solid Earth*, 99(B3):4969–4984.
- Corliss, J. B., Dymond, J., Gordon, L. I., Edmond, J. M., von Herzen, R. P., Ballard, R. D., Green, K., Williams, D., Bainbridge, A., Crane, K., et al. (1979). Submarine thermal springs on the galapagos rift. *Science*, 203(4385):1073–1083.
- Cowen, J. P., Wen, X., and Popp, B. N. (2002). Methane in aging hydrothermal plumes. *Geochimica et Cosmochimica Acta*, 66(20):3563–3571.

- Dick, G. J., Anantharaman, K., Baker, B. J., Li, M., Reed, D. C., and Sheik, C. S. (2013). The microbiology of deep-sea hydrothermal vent plumes: ecological and biogeographic linkages to seafloor and water column habitats. *Frontiers in Microbiology*, 4:124.
- Feely, R. A., Massoth, G. J., Baker, E. T., Lebon, G. T., and Geiselman, T. L. (1992). Tracking the dispersal of hydrothermal plumes from the Juan de Fuca Ridge using suspended matter compositions. *Journal of Geophysical Research: Solid Earth*, 97(B3):3457–3468.
- Flaspohler, G., Preston, V., Michel, A. P., Girdhar, Y., and Roy, N. (2019). Information-guided robotic maximum seek-and-sample in partially observable continuous environments. *IEEE Robotics and Automation Letters*, pages 3782–3789.
- Geilert, S., Hensen, C., Schmidt, M., Liebetrau, V., Scholz, F., Doll, M., Deng, L., Fiskal, A., Lever, M. A., Su, C.-C., et al. (2018). On the formation of hydrothermal vents and cold seeps in the Guaymas Basin, Gulf of California. *Biogeosciences*, 15(18):5715–5731.
- Georgieva, M. N., Little, C. T., Maslennikov, V. V., Glover, A. G., Ayupova, N. R., and Herrington, R. J. (2021). The history of life at hydrothermal vents. *Earth-Science Reviews*, 217:103602.
- Grassle, J. F. (1987). The ecology of deep-sea hydrothermal vent communities. In *Advances in Marine Biology*, volume 23, pages 301–362. Elsevier.
- Harb, C. C., Boyson, T. K., Kallapur, A. G., Petersen, I. R., Calzada, M. E., Spence, T. G., Kirkbride, K. P., and Moore, D. S. (2012). Pulsed quantum cascade laser-based CRDS substance detection: real-time detection of TNT. *Opt. Express*, 20(14):15489–15502.
- Holmes, R. M., Aminot, A., Kérout, R., Hooker, B. A., and Peterson, B. J. (1999). A simple and precise method for measuring ammonium in marine and freshwater ecosystems. *Canadian Journal of Fisheries and Aquatic Sciences*, 56(10):1801–1808.
- Jakuba, M. V. (2007). *Stochastic mapping for chemical plume source localization with application to autonomous hydrothermal vent discovery*. PhD thesis, Massachusetts Institute of Technology.
- Kapit, J. and Michel, A. P. (2021a). Dissolved gas sensing using an anti-resonant hollow core optical fiber. *Applied Optics*, 60(33):10354–10358.
- Kapit, J. and Michel, A. P. (2021b). Measurement of dissolved gases using a hollow core optical fiber and capillary membrane inlet. In *CLEO: Applications and Technology*, pages AM3Q–3. Optical Society of America.

- Le Bris, N., Yücel, M., Das, A., Sievert, S. M., LokaBharathi, P., and Girguis, P. R. (2019). Hydrothermal energy transfer and organic carbon production at the deep seafloor. *Frontiers in Marine Science*, 5:531.
- Lonsdale, P. and Becker, K. (1985). Hydrothermal plumes, hot springs, and conductive heat flow in the Southern Trough of Guaymas Basin. *Earth and Planetary Science Letters*, 73(2-4):211–225.
- Michel, A. P., Kapit, J., Colson, B., Pardis, W., Preston, V., Youngs, S., Uecker, L., Ruwini, R., Moya, Z., Roberts, J., Rawson, T., Hemp, P., Harb, C., Wankel, S., and Flaspoehler, G. (2022). Gas sensing in the deep ocean: advancing our ability to chemically explore. Ocean Science Meeting 2022.
- Michel, A. P., Preston, V. L., Fauria, K. E., and Nicholson, D. P. (2021). Observations of shallow methane bubble emissions from Cascadia margin. *Frontiers in Earth Science*, 9:613234.
- Miloshevich, L. M., Paukkunen, A., Vömel, H., and Oltmans, S. J. (2004). Development and validation of a time-lag correction for Vaisala radiosonde humidity measurements. *Journal of Atmospheric and Oceanic Technology*, 21(9):1305–1327.
- Morton, B., Taylor, G. I., and Turner, J. S. (1956). Turbulent gravitational convection from maintained and instantaneous sources. *Proceedings of the Royal Society of London. Series A. Mathematical and Physical Sciences*, pages 1–23.
- Ondréas, H., Scalabrin, C., Fouquet, Y., and Godfroy, A. (2018). Recent high-resolution mapping of Guaymas hydrothermal fields (Southern Trough). *Bulletin de la Société Géologique de France*, 189(1).
- Resing, J. A., Sedwick, P. N., German, C. R., Jenkins, W. J., Moffett, J. W., Sohst, B. M., and Tagliabue, A. (2015). Basin-scale transport of hydrothermal dissolved metals across the South Pacific Ocean. *Nature*, 523(7559):200–203.
- Särkkä, S. (2013). *Bayesian filtering and smoothing*. Number 3. Cambridge university press.
- Scholz, F., Schmidt, M., Hensen, C., Eroglu, S., Geilert, S., Gutjahr, M., and Liebetrau, V. (2019). Shelf-to-basin iron shuttle in the Guaymas Basin, Gulf of California. *Geochimica et Cosmochimica Acta*, 261:76–92.
- Seewald, J. S., Seyfried Jr, W. E., and Shanks III, W. C. (1994). Variations in the chemical and stable isotope composition of carbon and sulfur species during organic-rich sediment alteration: an experimental and theoretical study of hydrothermal activity at Guaymas Basin, Gulf of California. *Geochimica et Cosmochimica Acta*, 58(22):5065–5082.
- Silver, D. and Veness, J. (2010). Monte-Carlo planning in large POMDPs. In *Proc. Adv. Neural Inf. Process. Syst.*, pages 2164–2172.

- Soule, S. A., Seewald, J., Wankel, S. D., Michel, A., Beinart, R., Briones, E. E., Dominguez, E. M., Girguis, P., Coleman, D., Raineault, N. A., et al. (2018). Exploration of the Northern Guaymas Basin. *Oceanography*, 31(1):39–41.
- Speer, K. G. and Rona, P. A. (1989). A model of an atlantic and pacific hydrothermal plume. *Journal of Geophysical Research: Oceans*, 94(C5):6213–6220.
- Taylor, B. W., Keep, C. F., Hall Jr, R. O., Koch, B. J., Tronstad, L. M., Flecker, A. S., and Ulseth, A. J. (2007). Improving the fluorometric ammonium method: matrix effects, background fluorescence, and standard additions. *Journal of the North American Benthological Society*, 26(2):167–177.
- Teske, A., De Beer, D., McKay, L. J., Tivey, M. K., Biddle, J. F., Hoer, D., Lloyd, K. G., Lever, M. A., Røy, H., Albert, D. B., et al. (2016). The Guaymas Basin hiking guide to hydrothermal mounds, chimneys, and microbial mats: Complex seafloor expressions of subsurface hydrothermal circulation. *Frontiers in Microbiology*, 7:75.
- Tohidi, A. and Kaye, N. B. (2016). Highly buoyant bent-over plumes in a boundary layer. *Atmospheric Environment*, 131:97–114.
- Vic, C., Gula, J., Roullet, G., and Pradillon, F. (2018). Dispersion of deep-sea hydrothermal vent effluents and larvae by submesoscale and tidal currents. *Deep Sea Research Part I: Oceanographic Research Papers*, 133:1–18.
- Von Damm, K., Edmond, J. t., Measures, C., and Grant, B. (1985). Chemistry of submarine hydrothermal solutions at Guaymas Basin, Gulf of California. *Geochimica et Cosmochimica Acta*, 49(11):2221–2237.
- Wang, L., Pang, S., and Xu, G. (2020). 3-dimensional hydrothermal vent localization based on chemical plume tracing. In *Global Oceans 2020: Singapore–US Gulf Coast*, pages 1–7. IEEE.
- Welch, G., Bishop, G., et al. (1995). An introduction to the kalman filter.
- Yoerger, D. R., Bradley, A. M., Jakuba, M., German, C. R., Shank, T., and Tivey, M. (2007). Autonomous and remotely operated vehicle technology for hydrothermal vent discovery, exploration, and sampling. *Oceanography*, 20(1):152–161.